

Primal-mixed formulations for reaction–diffusion systems on deforming domains



Ricardo Ruiz-Baier

Institute of Earth Sciences, Géopolis UNIL-Mouline, University of Lausanne, CH-1015 Lausanne, Switzerland

ARTICLE INFO

Article history:

Received 13 December 2014

Received in revised form 8 June 2015

Accepted 10 July 2015

Available online 15 July 2015

Keywords:

Mixed finite elements

Reaction–diffusion systems

Excitable media

Moving domains

Linear and nonlinear elasticity

Single cell mechanics

Active strain

ABSTRACT

We propose a finite element formulation for a coupled elasticity–reaction–diffusion system written in a fully Lagrangian form and governing the spatio-temporal interaction of species inside an elastic, or hyper-elastic body. A primal weak formulation is the baseline model for the reaction–diffusion system written in the deformed domain, and a finite element method with piecewise linear approximations is employed for its spatial discretization. On the other hand, the strain is introduced as mixed variable in the equations of elastodynamics, which in turn acts as coupling field needed to update the diffusion tensor of the modified reaction–diffusion system written in a deformed domain. The discrete mechanical problem yields a mixed finite element scheme based on row-wise Raviart–Thomas elements for stresses, Brezzi–Douglas–Marini elements for displacements, and piecewise constant pressure approximations. The application of the present framework in the study of several coupled biological systems on deforming geometries in two and three spatial dimensions is discussed, and some illustrative examples are provided and extensively analyzed.

© 2015 Elsevier Inc. All rights reserved.

1. Introduction

Scope. We focus our attention in the numerical approximation of the chemical interaction between species concentrations and the response of the deformable medium where they react. Such a general framework is relevant to a wide range of applications going from molecular to macroscopic biological systems, and including, for instance, chemotaxis [52], organogenesis [41], bone remodelling [50,61], swelling of porous materials [38], cardiac electromechanics [31], tumor growth [10], force generation in skeletal muscle [15], wound healing [8], collagen network generation [34], tissue engineering [40], and many others.

The spatio-temporal dynamics of N species can be represented by a reaction–diffusion system of N equations, and the motion of the elastic (or hyper-elastic) medium in its general form, can be typically set in the framework of continuum mechanics, and thus be governed by the equations of elastodynamics. Much of the classical work in this particular field focuses in specific instances (such as radial growth or uniaxial contraction in simple domains) where it is possible to characterize the body motion without resolving the underlying solid mechanics and yielding reaction terms written directly in terms of growth rate (see e.g. [14] and the references therein). Nevertheless here we are interested in problems where the type of movement is not known a priori and therefore both the deformation and the deformation gradients are needed to describe the kinematics of the system: roughly speaking, the displacements/deformations are employed to update the

E-mail address: ricardo.ruizbaier@unil.ch.

position of the domain, and their gradients appear explicitly in the diffusive terms and are required in the formulation of reaction-diffusion systems written in a deformed medium.

Our primary goal is to introduce, implement, and apply a primal-mixed finite element formulation for the discretization of the coupled problem, where by *primal-mixed* we mean that the elasticity equations are set in a mixed form (that is, the associated formulation possesses a saddle-point structure involving additional unknowns) whereas the weak formulation of the reaction-diffusion sub-problem is written in terms of the primal variables only. From a discretization viewpoint, the clear advantages of a mixed formulation are that certain quantities of interest (such as strains or deformation gradients, which are needed in particular in the coupling strategy) can be immediately available with no need of further numerical differentiation, and that there exists more flexibility in the choice of finite element spaces. Moreover, mixed finite elements are the natural candidates for the discretization of the equations of incompressible elasticity, since the formal difficulties associated to infinite Lamé coefficients are absent. On the other hand, we are not particularly interested in recovering the species concentration fluxes and therefore we concentrate on primal formulations for the reaction-diffusion systems written in the deformed domain.

Related work. Traveling wave solutions for somewhat similar systems have been studied in [27]. A mechano-chemical cell aggregation model was developed in [57] under the assumption of infinitesimal strains of the medium, that allows to establish an equivalence relation between the reference and deformed domains, and that circumvents the difficulties associated to unknown body motion or nonlinear inter-configuration mappings. We also mention the finite element formulation for organogenesis based on a creeping flow description of the cartilage material presented in [42], and the discontinuous Galerkin approximation on moving grids and associated integration factor methods introduced in [62,12] to simulate limb pattern formation. Instead of using continuum-mechanics-based formulations, the elastodynamics can be alternatively represented with discrete models (as the mass-lattice model advanced in [58]). Models of cardiac electromechanics exhibit a remarkably similar structure, and several different formulations and solution techniques have been introduced in e.g. [13, 23,31,47]. Other related contributions include Eulerian formulations for wound healing [8], spherical tumor expansion [10], level-set and remeshed particle methods for surface and volume deformation [5,33,54], and many other approaches for different variants of growth in living tissues (see for instance, the recent review [32]). Nevertheless, none of these studies addresses primal-mixed methods in the spirit of the present basic idea.

Specific aims of this paper include:

- To introduce a mixed-primal formulation for a coupled Lagrangian elastodynamics-reaction-diffusion system where the mixed problem associated to the elasticity equations is written in terms of strains and deformations, and where the strain conveniently enters in the primal formulation of the reaction-diffusion system
- to develop a robust mixed finite element method suitable for the numerical study of a large class of coupled reaction-diffusion systems in elastic and hyperelastic domains
- to present separate formulations for linear and nonlinear mechanics
- to model the influence of reacting species into body deformation employing either a forcing term depending on the species concentration gradient, or an active strain decomposition.

Natural applications for the proposed framework are cardiac chemo- and electro-mechanical problems, however the present method is general enough to accommodate the study of many other related systems in biology and engineering.

Outline. We have arranged the contents of this paper in the following manner. Section 2 presents the derivation of the reaction-diffusion-elasticity equations, where the mechanics of the medium is specified in two cases: a linear and a non-linear hyperelastic material law. We recall some properties of the split systems and we introduce two primal-mixed weak formulations associated to the original coupled problem. In Section 3 we formulate the spatio-temporal discrete set of equations to be solved, its linearization via a Newton method, and we specify the choice of time advancing strategy and finite element spaces. Some numerical examples are given in Section 4, including accuracy assessment and several applications related to cardiac chemo-mechanics. We close with some remarks and perspectives collected in Section 5.

2. Reaction-diffusion equations on a deformable domain

2.1. Kinematics, motion and deformation

Let $\Omega_0 \subset \mathbb{R}^d$, $d \in \{2, 3\}$ denote an elastic body with polyhedral boundary $\partial\Omega_0$, regarded in its undeformed reference configuration, and denote by ν the outward unit normal vector on $\partial\Omega_0$. We assume a splitting of the boundary $\partial\Omega_0 = \overline{\Gamma_0^D} \cup \overline{\Gamma_0^N}$ into parts Γ_0^D and Γ_0^N where boundary loads and boundary tractions are imposed, respectively. A material point in Ω_0 is denoted by \mathbf{x} , whereas $\mathbf{u} : \Omega_0 \rightarrow \mathbb{R}^d$ denotes the deformation field that provides its position \mathbf{x}_t within the body Ω_t in the current configuration, and $\hat{\mathbf{v}} = \partial_t \hat{\mathbf{u}}|_{\mathbf{x}}$ is the (referential) velocity. The tensor $\mathbf{F} := \nabla \mathbf{u}$ is the gradient (applied with respect to the fixed material coordinates) of the deformation map, and $\mathbf{E}(\mathbf{u}) = \frac{1}{2}[\mathbf{F}^T \mathbf{F} - \mathbf{I}]$, $\mathbf{e}(\mathbf{u}) := \frac{1}{2}[\mathbf{F} + \mathbf{F}^T]$ denote the Green-Lagrange and the infinitesimal strain tensors, respectively. The symbols ∇_t , \mathbf{div}_t will stand for the gradient and

divergence operators taken with respect to the spatial coordinates \mathbf{x}_t . As usual, \mathbf{I} is the $d \times d$ identity tensor, and we recall that gradient operators in the actual and undeformed configurations are connected by the relation $\nabla_t(\cdot) = \mathbf{F}^{-\top} \nabla(\cdot)$.

In general, we will be mostly interested in the case where the material is (fully) incompressible, represented by the constraint

$$J(\mathbf{u}) := \det \mathbf{F} = 1$$

(or equivalently $\operatorname{div}_t \hat{\mathbf{v}} = 0$) which is enforced by the use of a Lagrange multiplier p , interpreted as the hydrostatic pressure field; and where the material exhibits a hyperelastic mechanical response. Under the assumption of small strains, the incompressibility condition boils down to

$$\operatorname{tr} \boldsymbol{\epsilon}(\mathbf{u}) = \operatorname{div} \mathbf{u} = 0.$$

We concentrate the presentation for two particular cases: a linear Saint Venant–Kirchhoff and a nonlinear Neo-Hookean material, whose behavior can be completely described by the strain (or free energy density) functions

$$\begin{aligned} \Psi(\mathbf{F}(\mathbf{u})) &= \frac{\lambda}{2} [\operatorname{tr} \boldsymbol{\epsilon}(\mathbf{u})]^2 + \mu \boldsymbol{\epsilon}(\mathbf{u}) : \boldsymbol{\epsilon}(\mathbf{u}), \\ \text{and } \Psi(\mathbf{F}(\mathbf{u})) &= \lambda \operatorname{tr} \mathbf{E} + \frac{\mu}{2} (J(\mathbf{u}) - 1)^2, \end{aligned}$$

respectively (see e.g. [6]), where λ, μ stand for the Lamé moduli in the context of the linear material, and (clearly making abuse of notation) also for the shear and bulk moduli in the Neo-Hookean case, respectively. The hydrostatic pressure and the first Piola–Kirchhoff stress tensor read respectively in each case

$$\begin{aligned} \frac{p}{\lambda} = \mathcal{P}(\mathbf{u}) &= \begin{cases} \operatorname{div} \mathbf{u}, \\ J(\mathbf{u}) - 1, \end{cases} \\ \text{and } \boldsymbol{\sigma}(\mathbf{u}, p) = \frac{\partial \Psi}{\partial \mathbf{F}} &= \begin{cases} 2\mu \boldsymbol{\epsilon} + p \mathbf{I}, \\ 2\mu \mathbf{F} + p J(\mathbf{u}) \mathbf{F}^{-\top}. \end{cases} \end{aligned}$$

The constitutive equation along with balances of mass and momentum are collected in the following system, written in total Lagrangian formulation

$$\boldsymbol{\sigma}(\mathbf{u}, p) = \frac{\partial \Psi}{\partial \mathbf{F}} \quad \text{in } \Omega_0 \times (0, T), \tag{2.1a}$$

$$\frac{1}{\lambda} p = \mathcal{P}(\mathbf{u}) \quad \text{in } \Omega_0 \times (0, T), \tag{2.1b}$$

$$\partial_{tt} \mathbf{u} - \operatorname{div} \boldsymbol{\sigma}(\mathbf{u}, p) = \mathbf{f}(s) \quad \text{in } \Omega_0 \times (0, T), \tag{2.1c}$$

$$\boldsymbol{\sigma} \mathbf{v} = \mathbf{g}_N \quad \text{on } \Gamma_0^N \times (0, T), \tag{2.1d}$$

$$\mathbf{u} = \mathbf{g}_D \quad \text{on } \Gamma_0^D \times (0, T). \tag{2.1e}$$

Notice that the motion of the body is assumed to be weakly influenced by pressure-like internal reactions encoded as a smooth body force being directly proportional to the local (material) gradient of scalar fields s_1, s_2, \dots to be made precise later:

$$\mathbf{f} := \mathbf{f}(s_1, \nabla s_1, s_2, \nabla s_2, \dots).$$

Remark 1 (*Active contraction*). In some circumstances the internal chemical reactions strongly affect the body motion, such as in active muscle contraction. In these situations a weak coupling needs to be replaced by e.g. an active-strain approach (see [45,53] for examples in cardiac electromechanics and developmental modeling, respectively), where it is assumed that the deformation gradient \mathbf{F} can be rewritten in terms of a Kröner–Lee multiplicative decomposition

$$\mathbf{F} = \mathbf{F}_e \mathbf{F}_o, \tag{2.2}$$

where \mathbf{F}_o is the active deformation tensor (here representing growth or contraction), to be constitutively prescribed by the scalar fields s_i (denoting for instance, species concentrations), and \mathbf{F}_e is the passive elastic deformation tensor, or instantaneous accommodation tensor of the body in a virtual intermediate configuration. Such a splitting is well-known in many constitutive theories (see for instance, the review in [36]).

Defining the variables $\gamma_f, \gamma_s, \gamma_n$ as the relative displacements in the orthonormal directions $\mathbf{f}_0, \mathbf{s}_0, \mathbf{n}_0$ of a contracting unit of the body, respectively, the *local* deformation is

$$\mathbf{F}_o = \mathbf{I} + \gamma_f \mathbf{f}_0 \otimes \mathbf{f}_0 + \gamma_s \mathbf{s}_0 \otimes \mathbf{s}_0 + \gamma_n \mathbf{n}_0 \otimes \mathbf{n}_0.$$

Notice that γ_f represents the active growth or active shortening of the body contracting units, whereas γ_s, γ_n will take into account the associated thickening or shrinking, in order to obey material incompressibility. The thermodynamic assumption

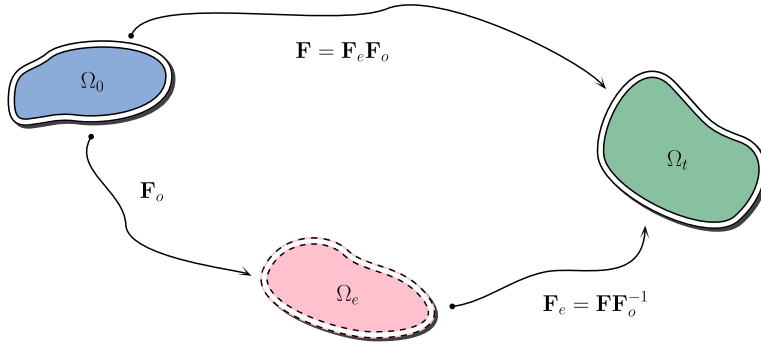


Fig. 1. Active strain decomposition entailing the introduction of a virtual intermediate configuration Ω_e between the reference and current states.

of the multiplicative decomposition (2.2) is that the active deformation \mathbf{F}_o stores no energy, so that the strain energy function in the intermediate configuration (see sketch in Fig. 1) is $\widehat{\Psi} = \Psi(\mathbf{F}_e)$. Finally, a pull-back to the reference configuration yields

$$\Psi_{\text{strain}} = \det \mathbf{F}_o \widehat{\Psi} = \det \mathbf{F}_o \Psi(\mathbf{F} \mathbf{F}_o^{-1}),$$

which in turn implies that (2.1) is replaced by

$$\begin{aligned} \boldsymbol{\sigma}(\mathbf{u}, p, \boldsymbol{\gamma}) &= \frac{\partial \det \mathbf{F}_o \Psi(\mathbf{F} \mathbf{F}_o^{-1})}{\partial \mathbf{F}}, \\ \frac{1}{\lambda} p &= \mathcal{P}(\mathbf{u}), \\ \partial_t \boldsymbol{\gamma} &= K(\boldsymbol{\gamma}, s), \\ \partial_{tt} \mathbf{u} - \mathbf{div} \boldsymbol{\sigma}(\mathbf{u}, p, \boldsymbol{\gamma}) &= \mathbf{f}(s), \\ \boldsymbol{\sigma} \mathbf{v} &= \mathbf{g}_{\mathbf{N}}, \\ \mathbf{u} &= \mathbf{g}_{\mathbf{D}}, \end{aligned} \tag{2.3}$$

where $\boldsymbol{\gamma} = (\gamma_f, \gamma_s, \gamma_n)$ and the third equation stands for the constitutive equation for the local active strain and its rate (see examples of specifications for K in e.g. [21]).

Remark 2 (*Pressure elimination*). Incompressibility is a typical assumption in the modeling of soft biological tissues, partially justified by the high percentage of water in the cells and proportionally low compressibility of extracellular constituents [2]. If in addition we consider a Saint Venant–Kirchhoff material in spatial dimension d , then (2.1a) and (2.1b) can be replaced, respectively, by

$$\boldsymbol{\sigma} = 2\mu \boldsymbol{\epsilon}(\mathbf{u}) + p \mathbf{I} \quad \text{and} \quad p - \frac{1}{d} \operatorname{tr} \boldsymbol{\sigma} = 0 \quad \text{in } \Omega_0 \times (0, T),$$

which implies that we can eliminate p from the first equation, yielding

$$\frac{1}{2\mu} \boldsymbol{\sigma}^d = \boldsymbol{\epsilon}(\mathbf{u}) \quad \text{in } \Omega_0 \times (0, T),$$

where $\boldsymbol{\tau}^d := \boldsymbol{\tau} - \frac{1}{d} \operatorname{tr} \boldsymbol{\tau} \mathbf{I}$ for all $\boldsymbol{\tau} \in \mathbb{L}^2(\Omega_0)$ (see e.g. [19]).

Remark 3 (*Stress splitting*). In the case of Neo-Hookean materials, and also for sake of the mixed formulation in mind, we can replace (2.1a) and (2.1c) by

$$\frac{1}{2\mu} \tilde{\boldsymbol{\sigma}} = \mathbf{F}, \quad \text{and} \quad -\partial_{tt} \mathbf{u} + \mathbf{div} \tilde{\boldsymbol{\sigma}} - \mathbf{div}[p J(\mathbf{u}) \mathbf{F}^{-t}] = -\mathbf{f}(s),$$

in $\Omega_0 \times (0, T)$, respectively.

Existence of solutions to (2.1) has been established in e.g. [35] for displacement-pressure formulations, based on classical arguments of polyconvexity of the strain energy and the implicit function theorem. For instance, discontinuous Galerkin formulations for (2.1) and (2.3) have been introduced and analyzed in [59,3], respectively.

2.2. Mixed formulations for elasticity

From now on, standard notation will be adopted for Lebesgue spaces $L^p(\Omega_0)$ and Sobolev spaces $H^s(\Omega_0)$ with norm $\|\cdot\|_{s,\Omega_0}$. By \mathbf{M}, \mathbb{M} we will denote the corresponding vectorial and tensorial counterparts of the generic scalar functional space M . We define the spaces $\mathbf{H}_D^1(\Omega_0) = \{\mathbf{v} \in \mathbf{H}^1(\Omega_0) : \mathbf{v}|_{\Gamma^D} = \mathbf{g}_D\}$, $\mathbf{H}_{D,0}^1(\Omega_0) = \{\mathbf{v} \in \mathbf{H}^1(\Omega_0) : \mathbf{v}|_{\Gamma^D} = \mathbf{0}\}$, and we recall that the space

$$\mathbb{H}(\mathbf{div}; \Omega_0) := \{\boldsymbol{\tau} \in \mathbb{L}^2(\Omega_0) : \mathbf{div} \boldsymbol{\tau} \in \mathbf{L}^2(\Omega_0)\},$$

equipped with the usual norm $\|\boldsymbol{\tau}\|_{\mathbf{div}, \Omega_0}^2 := \|\boldsymbol{\tau}\|_{0, \Omega_0}^2 + \|\mathbf{div}(\boldsymbol{\tau})\|_{0, \Omega_0}^2$ is a Hilbert space, and we introduce

$$\mathbb{H}_N(\mathbf{div}; \Omega_0) := \{\boldsymbol{\tau} \in \mathbb{H}(\mathbf{div}; \Omega_0) : \boldsymbol{\tau} \mathbf{v} = \mathbf{0} \text{ on } \Gamma_0^N\}.$$

Multiplying the nonlinear, coupled equations (2.1) by suitable test functions, integrating by parts over Ω_0 , and using Remark 3 we arrive at the following variational form of the model problem with Neo-Hookean elasticity:

For any $t > 0$, find $(\tilde{\sigma}(t), \mathbf{u}(t), p) \in \mathbb{H}_N(\mathbf{div}; \Omega_0) \times \mathbf{H}_D^1(\Omega_0) \times L^2(\Omega_0)$ satisfying

$$\begin{aligned} \frac{1}{2\mu} \int_{\Omega_0} \tilde{\sigma}(t) : \boldsymbol{\tau} + \int_{\Omega_0} \mathbf{u}(t) \cdot \mathbf{div} \boldsymbol{\tau} &= \int_{\Gamma_0^D} \mathbf{g}_D \cdot [\boldsymbol{\tau} \mathbf{v}], \\ \int_{\Omega_0} \mathbf{v} \cdot \mathbf{div} \tilde{\sigma}(t) - \int_{\Omega_0} \partial_{tt} \mathbf{u}(t) \cdot \mathbf{v} - \int_{\Omega_0} p J(\mathbf{u}) \nabla \mathbf{u}^{-t} : \nabla \mathbf{v} &= - \int_{\Omega_0} \mathbf{f} \cdot \mathbf{v}, \\ - \int_{\Omega_0} q [J(\mathbf{u}) - 1] + \frac{1}{\lambda} \int_{\Omega_0} pq &= 0, \end{aligned} \quad (2.4)$$

for all $(\boldsymbol{\tau}, \mathbf{v}, q) \in \mathbb{H}_N(\mathbf{div}; \Omega_0) \times \mathbf{H}_{D,0}^1(\Omega_0) \times L^2(\Omega_0)$.

For the linear Saint Venant-Kirchhoff material, and thanks to Remark 2, we can write (2.4) as:

Find $(\sigma(t), \mathbf{u}(t)) \in \mathbb{H}_N(\mathbf{div}; \Omega_0) \times \mathbf{H}_D^1(\Omega_0)$ such that

$$\begin{aligned} \frac{1}{2\mu} \int_{\Omega_0} \sigma^d(t) : \boldsymbol{\tau}^d + \int_{\Omega_0} \mathbf{u}(t) \cdot \mathbf{div} \boldsymbol{\tau} &= \int_{\Gamma_0^D} \mathbf{g}_D \cdot [\boldsymbol{\tau} \mathbf{v}], \quad \forall \boldsymbol{\tau} \in \mathbb{H}_N(\mathbf{div}; \Omega_0), \\ \int_{\Omega_0} \mathbf{v} \cdot \mathbf{div} \sigma(t) - \int_{\Omega_0} \partial_{tt} \mathbf{u}(t) \cdot \mathbf{v} &= - \int_{\Omega_0} \mathbf{f} \cdot \mathbf{v}, \quad \forall \mathbf{v} \in \mathbf{H}_{D,0}^1(\Omega_0). \end{aligned} \quad (2.5)$$

The (formal) matrix structures of (2.4) and (2.5) are respectively as follows

$$\underbrace{\begin{pmatrix} \mathcal{A} & \mathcal{B}^* & \mathbf{0} \\ \mathcal{B} & -\mathcal{C} & d\mathcal{E}_{\mathbf{u}} \\ \mathbf{0} & \mathcal{E}^* & \mathcal{S} \end{pmatrix}}_{\mathbb{M}_1} \begin{pmatrix} \tilde{\sigma} \\ \mathbf{u} \\ p \end{pmatrix} = \text{RHS}_1, \quad \underbrace{\begin{pmatrix} \mathcal{A} & \mathcal{B}^* \\ \mathcal{B} & -\mathcal{C} \end{pmatrix}}_{\mathbb{M}_2} \begin{pmatrix} \sigma^d \\ \mathbf{u} \end{pmatrix} = \text{RHS}_2, \quad (2.6)$$

where the involved linear and nonlinear operators $\mathcal{A} : \mathbb{H}_N(\mathbf{div}; \Omega_0) \rightarrow \mathbb{H}_N(\mathbf{div}; \Omega_0)', \mathcal{B} : \mathbb{H}_N(\mathbf{div}; \Omega_0) \rightarrow [\mathbf{H}_D^1(\Omega_0)]', \mathcal{B}^* : \mathbf{H}_D^1(\Omega_0) \rightarrow \mathbb{H}_N(\mathbf{div}; \Omega_0)', \mathcal{C} : \mathbf{H}_D^1(\Omega_0) \rightarrow [\mathbf{H}_D^1(\Omega_0)]', d\mathcal{E}_{\mathbf{u}} : L^2(\Omega_0) \rightarrow [\mathbf{H}_D^1(\Omega_0)]', \mathcal{E}^* : \mathbf{H}_D^1(\Omega_0) \rightarrow L^2(\Omega_0)', \mathcal{S} : L^2(\Omega_0) \rightarrow L^2(\Omega_0)'$ are defined by

$$[\mathcal{A}(\sigma), \boldsymbol{\tau}] := \frac{1}{2\mu} \int_{\Omega_0} \sigma : \boldsymbol{\tau}, \quad [\mathcal{B}(\sigma), \mathbf{v}] := \int_{\Omega_0} \mathbf{v} \cdot \mathbf{div} \sigma,$$

$$[\mathcal{B}^*(\mathbf{u}), \boldsymbol{\tau}] := \int_{\Omega_0} \mathbf{u} \cdot \mathbf{div} \boldsymbol{\tau}, \quad [\mathcal{C}(\mathbf{u}), \mathbf{v}] := \int_{\Omega_0} \partial_{tt} \mathbf{u} \cdot \mathbf{v},$$

$$[d\mathcal{E}_{\mathbf{u}}(p), \mathbf{v}] := - \int_{\Omega_0} p J(\mathbf{u}) \nabla \mathbf{u}^{-t} : \nabla \mathbf{v},$$

$$[\mathcal{E}(p), \mathbf{v}] := - \int_{\Omega_0} p [J(\mathbf{v}) - 1],$$

$$[\mathcal{E}^*(\mathbf{u}), q] := - \int_{\Omega_0} q [J(\mathbf{u}) - 1], \quad [\mathcal{S}(p), q] := \frac{1}{\lambda} \int_{\Omega_0} pq.$$

The motivation for the stress splitting of [Remark 3](#) becomes evident after observing the matrix structures in [\(2.6\)](#). Notice that \mathbb{M}_2 yields a linear saddle-point problem whose solvability depends on the coercivity of the diagonal forms in the kernel of \mathcal{B} and on adequate inf-sup conditions for \mathcal{B} . On the other hand, except for \mathcal{E} , the system with matrix \mathbb{M}_1 possesses the structure of a linear *twofold* saddle-point problem and it can be studied as in e.g. [\[18\]](#), where the analysis of a continuous problem and of mixed finite element formulations can be found (see also [\[20,28\]](#), where the theory is extended to nonlinear problems).

In the presence of the nonlinear maps \mathcal{E} and $d\mathcal{E}$, the system cannot be treated directly as a twofold saddle point with the arguments from [\[20\]](#), since the nonlinearity is not in the diagonal block of \mathbb{M}_1 . However, [\[35\]](#) presents a suitable framework where the conditions for existence of solutions are the ellipticity of \mathcal{A} , continuity of \mathcal{C} , appropriate inf-sup conditions for \mathcal{B} , continuous differentiability of \mathcal{E} in a neighborhood of \mathbf{u} and that its gradient $d\mathcal{E}$ has a splitting kernel and satisfies a suitable inf-sup condition.

2.3. Reaction-diffusion equations

For sake of simplicity we will restrict the discussion to reaction-diffusion systems describing the spatio-temporal interaction of the densities of two species w_1, w_2 , however the presentation is straightforwardly generalizable to the case of more species. Assuming that all constituent species are equi-present at each spatial point, the Reynolds transport theorem applied to the mass conservation of these species yields the following general and non-dimensional reaction-diffusion system for w_1, w_2 on a spatial (time-dependent) domain

$$\partial_t w_i + \hat{\mathbf{v}} \cdot \nabla_t w_i - \mathbf{div}_t(\mathbf{D}_i \nabla_t w_i) = H_i(w_1, w_2), \quad (2.7)$$

in $\Omega_t \times (0, T)$, for $i = 1, 2$, where $\mathbf{D}_i \in \mathbb{R}^{d \times d}$ is a tensor of (possibly anisotropic) diffusion rates and $H_i(w_1, w_2)$ are the reaction kinetics of the system representing the production and degradation of each species concentration. In this particular case, cross-diffusion effects are neglected and the coupling is present only in the reactive terms. Well-studied examples include the Schnakenberg model [\[51\]](#), the Gray-Scott model [\[25\]](#), and the FitzHugh-Nagumo equations [\[16,43\]](#), to name a few. Notice that the medium incompressibility has been already incorporated in [\(2.7\)](#) by assuming that $\mathbf{div}_t(\hat{\mathbf{v}} w_i) = \hat{\mathbf{v}} \cdot \nabla_t w_i$. A Lagrangian representation of the domain motion allows to rewrite the target system on a fixed domain in its reference configuration. Pulling back [\(2.7\)](#) to the initial configuration, using the Piola identity $\mathbf{div}(\mathbf{F}^{-t}) = 0$, applying the material incompressibility, and endowing the system with zero-flux boundary conditions, we arrive at

$$\begin{aligned} \partial_t w_i - \mathbf{div}(\mathbf{F}^{-1} \mathbf{D}_i \mathbf{F}^{-t} \nabla w_i) &= H_i(w_1, w_2) \quad \text{in } \Omega_0 \times (0, T), \text{ for } i = 1, 2, \\ \mathbf{F}^{-1} \mathbf{D}_i \mathbf{F}^{-t} \nabla w_i \cdot \mathbf{v} &= 0 \quad \text{on } \partial\Omega_0 \times (0, T), \text{ for } i = 1, 2. \end{aligned} \quad (2.8)$$

For a fixed domain (i.e. \mathbf{F} known), the positivity of initial data, the Lipschitz regularity of the reactive terms $H_i(\cdot, \cdot)$, and monotonicity of the diffusive term are sufficient to establish the existence and uniqueness of weak solutions to [\(2.8\)](#) (see e.g. [\[30\]](#), and the references therein). In addition, and depending on the specific form of the reaction kinetics $H_i(\cdot, \cdot)$, it is possible to derive so-called Turing conditions under which spatial patterns can emerge influenced by diffusion-driven instabilities [\[55\]](#). This is standard practice in fixed domains, however these conditions are quite different and maybe very difficult to obtain for moving domains, even for very specific types of movement (cf. [\[37\]](#)). Alternatively to [\(2.8\)](#), one could also devise a mixed formulation for the reaction-diffusion problem introducing the gradients of variables w_i as additional unknowns (see [\[29\]](#) for an application of gradient flows in cardiac electrophysiology), but in this context we are only interested in recovering the scalar primal fields.

2.4. Weak formulation for the coupled model problem

Multiplying [\(2.8\)](#) by suitable test functions, integrating by parts over Ω_0 , and putting the result together with [\(2.4\)](#), we arrive at the following primal-mixed variational form of the model problem with Neo-Hookean elasticity in terms of species concentration, strains, deformations and pressure:

For any $t > 0$, find $(w_1(t), w_2(t), \tilde{\sigma}(t), \mathbf{u}(t), p) \in \mathbf{H}^1(\Omega_0) \times \mathbf{H}^1(\Omega_0) \times \mathbb{H}_N(\mathbf{div}; \Omega_0) \times \mathbf{H}_D^1(\Omega_0) \times L^2(\Omega_0)$ satisfying

$$\begin{aligned} [\mathcal{W}_{\tilde{\sigma}}(w_1(t), w_2(t)), (s_1, s_2)] &= [\mathcal{H}(w_1(t), w_2(t)), (s_1, s_2)], \\ [\mathcal{A}(\tilde{\sigma}(t)), \boldsymbol{\tau}] + [\mathcal{B}^*(\mathbf{u}(t)), \boldsymbol{\tau}] &= \mathcal{G}(\boldsymbol{\tau}), \\ [\mathcal{B}(\tilde{\sigma}(t)), \mathbf{v}] - [\mathcal{C}(\mathbf{u}(t)), \mathbf{v}] + [d\mathcal{E}_{\mathbf{u}}(p), \mathbf{v}] &= [\mathcal{F}(w_1(t), w_2(t)), \mathbf{v}], \\ [\mathcal{E}^*(\mathbf{u}(t)), q] + [\mathcal{S}(p), q] &= 0, \end{aligned} \quad (2.9)$$

for all $(s_1, s_2, \boldsymbol{\tau}, \mathbf{v}, q) \in \mathbf{H}^1(\Omega_0) \times \mathbf{H}^1(\Omega_0) \times \mathbb{H}_N(\mathbf{div}; \Omega_0) \times \mathbf{H}_{D,0}^1(\Omega_0) \times L^2(\Omega_0)$, and where

$$[\mathcal{W}_{\tilde{\sigma}}(w_1, w_2), (s_1, s_2)] := \sum_{i=1}^2 \int_{\Omega_0} \partial_t w_i s_i + 4\mu^2 \int_{\Omega_0} \tilde{\sigma}^{-1} \mathbf{D}_i \tilde{\sigma}^{-t} \nabla w_i \cdot \nabla s_i, \quad \mathcal{G}(\boldsymbol{\tau}) := \int_{\Gamma_0^D} \mathbf{g}_D \cdot \boldsymbol{\tau} \mathbf{v},$$

$$[\mathcal{H}(w_1, w_2), (s_1, s_2)] := \sum_{i=1}^2 \int_{\Omega_0} H_i(w_1, w_2) s_i, \quad [\mathcal{F}(w_1, w_2), \mathbf{v}] := - \int_{\Omega_0} \mathbf{f}(w_1, w_2) \cdot \mathbf{v}.$$

An analogous system arises in the case of a linear Saint Venant–Kirchhoff material. Existence and uniqueness results for (2.9) are not yet available from the literature, and they currently go beyond the scope of the present paper. However a similar (linearized) system arising in the study of cardiac electromechanics has been recently studied in [1] using parabolic regularization, the Faedo–Galerkin method, and monotonicity–compactness arguments.

3. Discretization of the model problem

Here we focus on the space–time discretization of the coupled problem (2.9). A Rothe-type strategy is used, where we first apply a time discretization based on finite differences (in particular, the well-known BDF2 method), followed by the formulation of a primal-mixed finite element method for the spatial discretization.

3.1. Time discretization

The evolution in time is performed considering a uniform partition of the interval $[0, T]$ as $[0, \dots, t^n, \dots, t^N = T]$ into N subintervals of size Δt . We apply a second order backward difference advancing scheme (BDF2, see e.g. [26]): For given values of $w_i^0, w_i^{-1}, \sigma^0, \mathbf{u}^0, \mathbf{u}^{-1}, \mathbf{u}^{-2}, p^0$, and for $n = 0, 1, \dots$, find $(w_1^{n+1}, w_2^{n+1}, \sigma^{n+1}, \mathbf{u}^{n+1}, p^{n+1})$ such that

$$\begin{aligned} \sum_{i=1}^2 \frac{1}{\Delta t} (\dot{w}_i^{n+1}, s_i)_{\Omega_0} + 4\mu^2 (\tilde{\sigma}^{-1} \mathbf{D}_i \tilde{\sigma}^{-\top} \nabla w_i^{n+1}, \nabla s_i)_{\Omega_0} &= [\mathcal{H}(w_1^{n+1}, w_2^{n+1}), (s_1, s_2)], \\ [\mathcal{A}(\tilde{\sigma}^{n+1}), \boldsymbol{\tau}] + [\mathcal{B}^*(\mathbf{u}^{n+1}), \boldsymbol{\tau}] &= \mathcal{G}(\boldsymbol{\tau}), \\ [\mathcal{B}(\tilde{\sigma}^{n+1}), \mathbf{v}] - \frac{1}{(\Delta t)^2} (\ddot{\mathbf{u}}^{n+1}, \mathbf{v})_{\Omega_0} + [d\mathcal{E}_{\mathbf{u}^{n+1}}(p^{n+1}), \mathbf{v}] &= [\mathcal{F}(w_1^{n+1}, w_2^{n+1}), \mathbf{v}], \\ [\mathcal{E}^*(\mathbf{u}^{n+1}), q] + [\mathcal{S}(p^{n+1}), q] &= 0, \end{aligned}$$

for all $(s_1, s_2, \boldsymbol{\tau}, \mathbf{v}, q) \in H^1(\Omega_0) \times H^1(\Omega_0) \times \mathbb{H}_N(\mathbf{div}; \Omega_0) \times \mathbf{H}_{D,0}^1(\Omega_0) \times L^2(\Omega_0)$, where the dot and double dot symbols denote the second order BDF approximations of the first and second time derivatives, respectively, i.e.,

$$\begin{aligned} \dot{s}^{n+1} &:= \frac{3}{2}s^{n+1} - 2s^n + \frac{1}{2}s^{n-1}, \\ \ddot{\mathbf{v}}^{n+1} &:= 2\mathbf{v}^{n+1} - 5\mathbf{v}^n + 4\mathbf{v}^{n-1} - \mathbf{v}^{n-2}. \end{aligned}$$

Since the time advancing scheme is fully implicit, no CFL condition is required in principle. However, in all subsequent simulations, the time step will be heuristically chosen so that the underlying physics of each particular problem are not missed.

3.2. Space discretization

Let us denote by \mathcal{T}_h a regular simplicial partition of Ω_0 by triangles (for $d = 2$, or tetrahedra for $d = 3$) K of diameter h_K and define the meshsize as $h := \max\{h_K : K \in \mathcal{T}_h\}$. For the approximation of strains, deformations, species concentrations, and pressure, respectively, we will employ finite dimensional spaces $\mathbb{H}_h, \mathbf{V}_h, S_h, Q_h$ that we will specify later on. The fully-discrete counterpart of the nonlinear system (2.9) consists in solving

$$\begin{aligned} \sum_{i=1}^2 \frac{1}{\Delta t} (\dot{w}_{i,h}^{n+1}, s_i)_{\Omega_0} + 4\mu^2 (\tilde{\sigma}_h^{-1} \mathbf{D}_i \tilde{\sigma}_h^{-\top} \nabla w_{i,h}^{n+1}, \nabla s_i)_{\Omega_0} &= [\mathcal{H}(w_{1,h}^{n+1}, w_{2,h}^{n+1}), (s_1, s_2)], \\ [\mathcal{A}(\tilde{\sigma}_h^{n+1}), \boldsymbol{\tau}] + [\mathcal{B}^*(\mathbf{u}_h^{n+1}), \boldsymbol{\tau}] &= \mathcal{G}(\boldsymbol{\tau}), \\ [\mathcal{B}(\tilde{\sigma}_h^{n+1}), \mathbf{v}] - \frac{1}{(\Delta t)^2} (\ddot{\mathbf{u}}_h^{n+1}, \mathbf{v})_{\Omega_0} + [d\mathcal{E}_{\mathbf{u}_h^{n+1}}(p_h^{n+1}), \mathbf{v}] &= [\mathcal{F}(w_{1,h}^{n+1}, w_{2,h}^{n+1}), \mathbf{v}], \\ [\mathcal{E}^*(\mathbf{u}_h^{n+1}), q] + [\mathcal{S}(p_h^{n+1}), q] &= 0, \end{aligned} \tag{3.1}$$

for all $(s_1, s_2, \boldsymbol{\tau}, \mathbf{v}, q) \in S_h \times \mathbb{H}_h \times \mathbf{V}_h \times Q_h$ and for each $n = 0, 1, \dots$. In what follows, and whenever clear from the context, we will drop the superscript $n + 1$ corresponding to the current time step.

3.3. Consistent Newton–Raphson linearization

As long as we focus on Saint Venant–Kirchhoff materials, the only nonlinearities in (3.1) consist in the reaction and the coupling terms. For instance, a standard fixed point argument allows the decoupling of the governing equations and an abundant literature exists dedicated to the analysis and efficient mixed finite element discretization of linear elasticity, where the constitutive equation can be easily inverted (see e.g. [11], and the references therein). The scenario is less favorable for nonlinear materials and so we provide details on the Jacobian employed in the solution of the linearized equations. We will denote by $(\delta w_{1,h}, \delta w_{2,h}, \delta \tilde{\sigma}_h, \delta \mathbf{u}_h, \delta p_h)$ the incremental solutions to the following linearization of (3.1) around a generic state $(\hat{w}_{1,h}, \hat{w}_{2,h}, \hat{\tilde{\sigma}}_h, \hat{\mathbf{u}}_h, \hat{p}_h)$:

$$\begin{aligned} & \sum_{i=1}^2 \frac{3}{2\Delta t} (\delta w_{i,h} + \hat{w}_{i,h}, s_i)_{\Omega_0} - 4\mu^2 \sum_{i=1}^2 (\hat{\tilde{\sigma}}_h^{-1} \mathbf{D}_i \hat{\tilde{\sigma}}_h^{-\top} \delta \tilde{\sigma}_h^\top \hat{\tilde{\sigma}}_h^{-\top} \nabla \hat{w}_{i,h}, \nabla s_i)_{\Omega_0} \\ & + 4\mu^2 \sum_{i=1}^2 (\hat{\tilde{\sigma}}_h^{-1} \mathbf{D}_i \hat{\tilde{\sigma}}_h^{-\top} \nabla \delta w_{i,h}, \nabla s_i)_{\Omega_0} - 4\mu^2 \sum_{i=1}^2 (\hat{\tilde{\sigma}}_h^{-1} \delta \tilde{\sigma}_h \hat{\tilde{\sigma}}_h^{-1} \mathbf{D}_i \hat{\tilde{\sigma}}_h^{-\top} \nabla \hat{w}_{i,h}, \nabla s_i)_{\Omega_0} \\ & - \sum_{i=1}^2 \frac{1}{2\Delta t} (4\hat{w}_{i,h}^n - \hat{w}_{i,h}^{n-1}, s_i)_{\Omega_0} - [d\mathcal{H}(\delta w_{1,h}, \delta w_{2,h}), (s_1, s_2)] - [\mathcal{H}(\hat{w}_{1,h}, \hat{w}_{2,h}), (s_1, s_2)] = 0, \\ & [\mathcal{A}(\delta \tilde{\sigma}_h), \boldsymbol{\tau}] + [\mathcal{A}(\hat{\tilde{\sigma}}_h), \boldsymbol{\tau}] + [\mathcal{B}^*(\delta \mathbf{u}_h), \boldsymbol{\tau}] + [\mathcal{B}^*(\hat{\mathbf{u}}_h), \boldsymbol{\tau}] - \mathcal{G}(\boldsymbol{\tau}) = 0, \\ & [\mathcal{B}(\delta \sigma_h), \mathbf{v}] + [\mathcal{B}(\hat{\sigma}_h), \mathbf{v}] - \frac{2}{(\Delta t)^2} (\delta \mathbf{u}_h + \hat{\mathbf{u}}_h, \mathbf{v})_{\Omega_0} + [d\mathcal{E}_{\hat{\mathbf{u}}_h}(\delta p_h), \mathbf{v}] + [d^2\mathcal{E}_{\delta \mathbf{u}_h, \hat{\mathbf{u}}_h}(\hat{p}_h), \mathbf{v}] \\ & + [d\mathcal{E}_{\hat{\mathbf{u}}_h}(\hat{p}_h), \mathbf{v}] + \frac{1}{(\Delta t)^2} (5\mathbf{u}_h^n - 4\mathbf{u}_h^{n-1} + \mathbf{u}_h^{n-2}, \mathbf{v})_{\Omega_0} - [d\mathcal{F}(\delta w_{1,h}, \delta w_{2,h}), \mathbf{v}] \\ & - [\mathcal{F}(\hat{w}_{1,h}, \hat{w}_{2,h}), \mathbf{v}] = 0, \\ & [d\mathcal{E}^*(\delta \mathbf{u}_h), q] + [\mathcal{E}^*(\hat{\mathbf{u}}_h), q] + [\mathcal{S}(\delta p_h), q] + [\mathcal{S}(\hat{p}_h), q] = 0, \end{aligned} \quad (3.2)$$

for all $(\mathbf{s}, \boldsymbol{\tau}, \mathbf{v}, q) \in S_h \times \mathbb{H}_h \times \mathbf{V}_h \times Q_h$, where the (Gâteaux) derivatives appearing in (3.2), computed in the direction of the corresponding increments are

$$\begin{aligned} [d\mathcal{H}(\delta w_1, \delta w_2), (s_1, s_2)] &:= \sum_{i,j=1}^2 \int_{\Omega_0} \frac{d}{d\hat{w}_j} H_i(\hat{w}_1, \hat{w}_2) \delta w_j s_j, \\ [d\mathcal{F}(\delta w_1, \delta w_2), \mathbf{v}] &:= - \sum_{i=1}^2 \int_{\Omega_0} \delta w_i \frac{d}{d\hat{w}_i} \mathbf{f}(\hat{w}_1, \hat{w}_2) \cdot \mathbf{v}, \\ [d\mathcal{E}^*(\delta \mathbf{u}), q] &:= - \int_{\Omega_0} q J(\hat{\mathbf{u}}) \nabla \hat{\mathbf{u}}^{-\top} \operatorname{div}(\delta \mathbf{u}), \\ [d^2\mathcal{E}_{\delta \mathbf{u}, \hat{\mathbf{u}}}(\hat{p}), \mathbf{v}] &:= \int_{\Omega_0} \hat{p} J(\hat{\mathbf{u}}) \nabla \hat{\mathbf{u}}^{-\top} (\nabla \delta \mathbf{u} - \nabla \delta \mathbf{u}^\top) \nabla \hat{\mathbf{u}}^{-\top} : \nabla \mathbf{v}. \end{aligned}$$

Provided that the initial guess is sufficiently close to the updated solution, the use of the exact Jacobian ensures quadratic convergence of the Newton algorithm.

3.4. Finite element spaces

As usual, $\mathbb{P}_r(R)$ denotes the space of polynomial functions of degree $s \leq r$ defined on the set R . For each element $K \in \mathcal{T}_h$, we recall that the local Raviart–Thomas space of order k , $k \geq 0$ is defined as

$$\mathbb{RT}_k(K) = \mathbb{P}_k(K)^d \oplus \mathbb{P}_k(K)\mathbf{x},$$

for $\mathbf{x} \in \mathbb{R}^d$, the local Brezzi–Douglas–Marini space of order k is defined as

$$\mathbb{BDM}_k(K) = \mathbb{P}_k(K)^d \cap H(\operatorname{div}, K),$$

and we specify the finite element spaces $\mathbb{H}_h \subset \mathbb{H}_N(\operatorname{div}; \Omega_0)$, $\mathbf{V}_h \subset H(\operatorname{div}, \Omega_0)$, $S_h \subset H^1(\Omega_0)$, $Q_h \subset L^2(\Omega_0)$ for the approximation of strains, deformations, species concentrations, and pressure, respectively, as follows:

$$\begin{aligned}\mathbb{H}_h &:= \{\boldsymbol{\tau}_h \in \mathbb{H}_N(\mathbf{div}; \Omega_0) : (\tau_h^{i1}, \dots, \tau_h^{id})^\top \in \mathbb{RT}_k(K), \forall i \in \{1, \dots, d\}, \forall K \in \mathcal{T}_h\}, \\ \mathbf{V}_h &:= \{\mathbf{v}_h : \mathbf{v}_h|_K \in \mathbb{BDM}_{k+1}(K), \forall K \in \mathcal{T}_h\}, \\ S_h &:= \{s_h \in \mathbf{H}^1(\Omega_0) : s_h|_K \in \mathbb{P}_{k+1}(K), \forall K \in \mathcal{T}_h\}, \\ Q_h &:= \{q_h \in \mathbf{L}^2(\Omega_0) : q_h|_K \in \mathbb{P}_k(K), \forall K \in \mathcal{T}_h\}.\end{aligned}$$

Notice that for the linear elastic material, one could also employ $\mathbb{P}_k(K)^d$ elements (with arbitrary $k \geq 0$) for the approximation of the deformation field, since neither the gradient of trial nor tests deformations appear in the discrete formulation associated to (2.5).

Concentrating only on the hyperelasticity part of (3.2), we realize that its matrix structure assumes the form

$$\begin{pmatrix} \mathcal{A} & \mathcal{B}^* & \mathbf{0} \\ \mathcal{B} & -\mathcal{C} & \widehat{d\mathcal{E}} \\ \mathbf{0} & \widehat{d\mathcal{E}}^* & -\mathcal{S} \end{pmatrix} \begin{pmatrix} \delta\tilde{\boldsymbol{\sigma}}_h \\ \delta\mathbf{u}_h \\ \delta p_h \end{pmatrix} = \text{RHS}_3,$$

which is a linear problem for the solution increments, where RHS₃ contains body and boundary forces, the terms associated to the previous time steps, and the Newton residuals. Assuming enough regularity, this twofold saddle point system can be solved as long as \mathcal{A} is \mathbb{H}_h -elliptic, \mathcal{C} , \mathcal{S} are positive semi-definite, and \mathcal{B} , $\widehat{d\mathcal{E}}$ satisfy uniform inf-sup conditions on $\mathbb{H}_h \times \mathbf{V}_h$ and $\mathbf{V}_h \times Q_h$, respectively (see e.g. [20]).

Formally, expected convergence rates for the spatial approximation of the linearized coupled problem (3.2) will be optimally of order $k + 1$ in the natural norms (in the sense that they coincide with the interpolation properties of the specific spaces employed herein).

4. Numerical examples

This section contains an example assessing the experimental spatio-temporal convergence rate of the proposed primal-mixed method, plus some selected illustrative tests of high interest in the simulation of meso and macroscopic cardiac chemo-mechanics.

4.1. Accuracy tests

We first verify the spatial convergence of the proposed numerical scheme, restricting ourselves to the lowest order case ($k = 0$). We consider the following version of (2.9) defined on the unit disk $\Omega_0 = \{(x, y) : x^2 + y^2 \leq 1\}$ and for the time horizon $t \in (0, T = 1)$

$$\begin{aligned}\int_{\Omega_0} \partial_t w_1 s_1 + 4\mu^2 \int_{\Omega_0} \tilde{\boldsymbol{\sigma}}^{-1} \mathbf{D}_1 \tilde{\boldsymbol{\sigma}}^{-\top} \nabla w_1 \cdot \nabla s_1 - \int_{\Omega_0} w_1 s_1 &= \int_{\Omega_0} f_1 s_1, \\ \int_{\Omega_0} \partial_t w_2 s_2 + 4\mu^2 \int_{\Omega_0} \tilde{\boldsymbol{\sigma}}^{-1} \mathbf{D}_2 \tilde{\boldsymbol{\sigma}}^{-\top} \nabla w_2 \cdot \nabla s_2 - \int_{\Omega_0} w_2 s_2 &= \int_{\Omega_0} f_2 s_2, \\ [\mathcal{A}(\tilde{\boldsymbol{\sigma}}), \boldsymbol{\tau}] + [\mathcal{B}^*(\mathbf{u}), \boldsymbol{\tau}] &= \int_{\Gamma_0^D} \mathbf{g}_D \cdot [\boldsymbol{\tau} \mathbf{v}], \\ \int_{\Omega_0} \partial_{tt} \mathbf{u} \cdot \mathbf{v} + [\mathcal{B}(\tilde{\boldsymbol{\sigma}}), \mathbf{v}] + [d\mathcal{E}_{\mathbf{u}}(p), \mathbf{v}] + \int_{\Omega_0} \mathbf{f}(w_1, w_2) \cdot \mathbf{v} &= - \int_{\Omega_0} \mathbf{g} \cdot \mathbf{v}, \\ [\mathcal{E}^*(\mathbf{u}), q] + [\mathcal{S}(p), q] &= 0,\end{aligned}\tag{4.1}$$

which admits an exact solution given by

$$\begin{aligned}\mathbf{u} &= 2\mu \sin\left(\frac{\pi}{2}t\right) (-\sin(x)\cos(y), \cos(x)\sin(y))^\top, \\ p &= 4\mu^2 \pi^2 \sin^2\left(\frac{\pi}{2}t\right) (\sin^2(x)\sin^2(y) - \cos^2(x)\cos^2(y)), \\ w_1 &= \sin\left(\frac{\pi}{2}t\right) \exp(-x)\cos(y), \quad w_2 = \sin\left(\frac{\pi}{2}t\right) \exp(-y)\sin(x).\end{aligned}\tag{4.2}$$

We consider the material to be Neo-Hookean and choose $\lambda = 1$, $\mu = 0.09$, $\mathbf{f}(w_1, w_2) = w_1^2 w_2 - w_1 w_2^2$, while source terms f_1 , f_2 , \mathbf{g} and Dirichlet boundary conditions of the problem are adjusted according to these exact solutions. The computational domain is discretized on a family of unstructured triangular meshes having 2^{l+1} , $l = 0, 1, \dots$ nodes on the

Table 1

Spatial and temporal error history associated to the FEM-BDF2 discretization of the model problem, computed until a final time $T = 1$. Errors on the top rows were computed using a fixed time step of $\Delta = 0.001$, whereas those on the bottom rows were obtained on a fine mesh of size $h = 0.0109$.

Space convergence										
h	$e_h(w_1)$	$r_h(w_1)$	$e_h(w_2)$	$r_h(w_2)$	$e_h(\sigma)$	$r_h(\sigma)$	$e_h(\mathbf{u})$	$r_h(\mathbf{u})$	$e_h(p)$	$r_h(p)$
1.0017	2.6442	—	2.6530	—	0.8381	—	0.9533	—	0.2799	—
0.7534	2.1830	0.6725	2.1881	0.6769	0.6725	0.7724	0.7734	0.7347	0.2177	0.8824
0.3818	1.1361	0.9614	1.1360	0.9636	0.3467	0.9749	0.3983	0.9762	0.1119	0.8793
0.2037	0.6098	0.9899	0.6089	0.9929	0.1860	0.9909	0.2133	0.9937	0.0599	0.9243
0.1070	0.3211	0.9965	0.3209	0.9954	0.0979	0.9965	0.1123	0.9971	0.0315	0.8984
0.0561	0.1692	0.9921	0.1693	0.9898	0.0517	0.9887	0.0589	0.9981	0.0165	0.9397
0.0294	0.0907	0.9662	0.0906	0.9683	0.0278	0.9599	0.0311	0.9894	0.0086	0.9959
0.0167	0.0556	0.8632	0.0555	0.8662	0.0173	0.8352	0.0181	0.9547	0.0049	0.9637

Time convergence										
Δt	$e_{\Delta t}(w_1)$	$r_{\Delta t}(w_1)$	$e_{\Delta t}(w_2)$	$r_{\Delta t}(w_2)$	$e_{\Delta t}(\sigma)$	$r_{\Delta t}(\sigma)$	$e_{\Delta t}(\mathbf{u})$	$r_{\Delta t}(\mathbf{u})$	$e_{\Delta t}(p)$	$r_{\Delta t}(p)$
0.1000	194.56	—	187.80	—	55.278	—	62.409	—	21.698	—
0.0500	43.950	1.8210	41.730	1.8565	14.062	1.8874	16.385	1.9037	6.3712	1.9021
0.0250	11.162	1.9247	10.427	1.9082	3.5731	1.9250	4.8210	1.8978	1.6147	1.9574
0.0125	3.3217	1.8962	2.8633	1.8301	0.9013	1.8346	1.2367	1.9344	0.4258	1.9338
0.0062	0.8281	1.9615	0.8236	1.9803	0.2678	1.8804	0.4109	1.9486	0.1129	1.8076
0.0031	0.2152	1.8921	0.2231	1.8320	0.0680	1.8372	0.1063	1.9590	0.0253	1.9039
0.0017	0.0577	1.9187	0.0561	1.9473	0.0169	1.7471	0.0268	1.9332	0.0062	1.8894
0.0008	0.0142	1.9452	0.0141	1.9682	0.0043	1.9603	0.0065	1.9764	0.0016	1.9342

circle defining the domain boundary. Relative spatial errors and convergence rates between exact and approximate solutions in different norms are defined as

$$\begin{aligned} e_h(\sigma) &= \frac{\|\sigma(\cdot, T) - \sigma_h^N\|_{\text{div}, \Omega_0}}{\|\sigma(\cdot, T)\|_{\text{div}, \Omega_0}}, \quad e_h(\mathbf{u}) = \frac{\|\mathbf{u}(\cdot, T) - \mathbf{u}_h^N\|_{1, \Omega_0}}{\|\mathbf{u}(\cdot, T)\|_{1, \Omega_0}}, \\ e_h(w_i) &= \frac{\|w_i(\cdot, T) - w_{i,h}^N\|_{1, \Omega_0}}{\|w_i(\cdot, T)\|_{1, \Omega_0}}, \quad e_h(p) = \frac{\|p(\cdot, T) - p_h^N\|_{0, \Omega_0}}{\|p(\cdot, T)\|_{0, \Omega_0}}, \quad r_h(\cdot) = \frac{\log(e_h(\cdot)/\hat{e}_h(\cdot))}{\log(h/\hat{h})}, \end{aligned} \quad (4.3)$$

where e and \hat{e} denote errors generated on two consecutive meshes of sizes h and \hat{h} . These errors are computed using Gauss quadrature formulas that are, for the chosen approximation spaces, exact on each element. Here $q(\cdot, T)$ and q_h^N denote the continuous and discrete approximation of the generic field q evaluated at the final time $t^N = T$. We depict in Table 1 empirical relative errors and convergence rates (4.3) for the numerical solutions compared with respect to (4.2), as function of the meshsize h , where we observe first order convergence for all fields in their relevant norms. We also evidence a second order convergence rate for the time approximation of the problem when refining the timestep Δt . Errors associated to the temporal discretization of a generic field q are measured in the $\ell^\infty(0, T; \cdot)$ -norm, that is:

$$e_{\Delta t}(q) = \sum_{n=0}^N \|q(\cdot, t^n) - q_h^n\|_{i, \Omega}, \quad r_{\Delta t}(q) = \frac{\log(e_{\Delta t}(q)/\hat{e}_{\Delta t}(q))}{\log(\Delta t/\widehat{\Delta t})},$$

on successively refined partitions of $(0, T)$, where $i \in \{\text{div}, 0, 1\}$. Even if rigorous theoretical estimates are not yet available for problems like (4.1), related (continuous in time) results for elasticity, poroelasticity and cardiac mechanics [3,11,47,49,60] suggest that the obtained rates are optimal. At each Newton iteration the involved linear systems have been solved with the GMRES method (with a tolerance of $1e-7$), combined with Schwarz preconditioning. Fig. 2 displays a snapshot of the approximate solutions at the final time $T = 1$, obtained with the proposed mixed-primal formulation on a mesh generated after six levels of refinement (representing roughly 200K degrees of freedom).

4.2. Slow calcium waves in isolated cardiomyocytes

Simplified calcium-induced-calcium-release dynamics inside a single cardiac cell can be modeled with the following specification for the reaction terms [24], where w_1, w_2 represent the concentrations of cytosolic and sarcoplasmic calcium

$$\begin{aligned} H_1(w_1, w_2) &= \nu_1 - \frac{\nu_2 w_1^2}{k_2 + w_1^2} + \frac{\nu_3 w_1^4 w_2^2}{(k_3 + w_2^2)(k_4 + w_1^4)} - \nu_4 w_1, \\ H_2(w_1, w_2) &= \frac{\nu_2 w_1^2}{k_2 + w_1^2} - \frac{\nu_3 w_1^4 w_2^2}{(k_3 + w_2^2)(k_4 + w_1^4)} - \nu_5 w_1. \end{aligned} \quad (4.4)$$

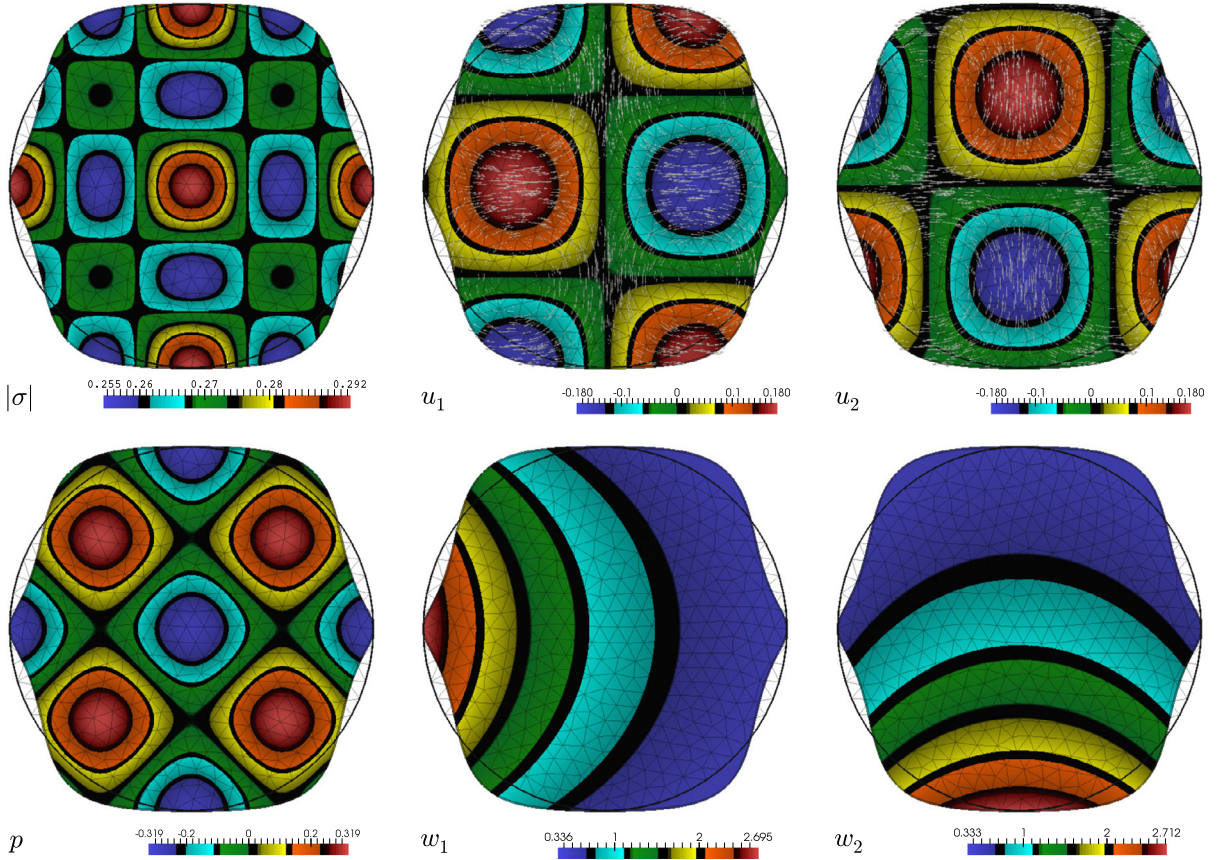


Fig. 2. Approximate norm of the Neo-Hookean stress tensor (top left), velocity components with vectors (top center and right), pressure profile (bottom left), and species concentrations (bottom center and right) for the spatio-temporal accuracy test, all rendered on the deformed domain Ω_t , and computed at the final time $T = 1$. For sake of visualization we also depict a coarse mesh of the reference disk-shaped domain Ω_0 .

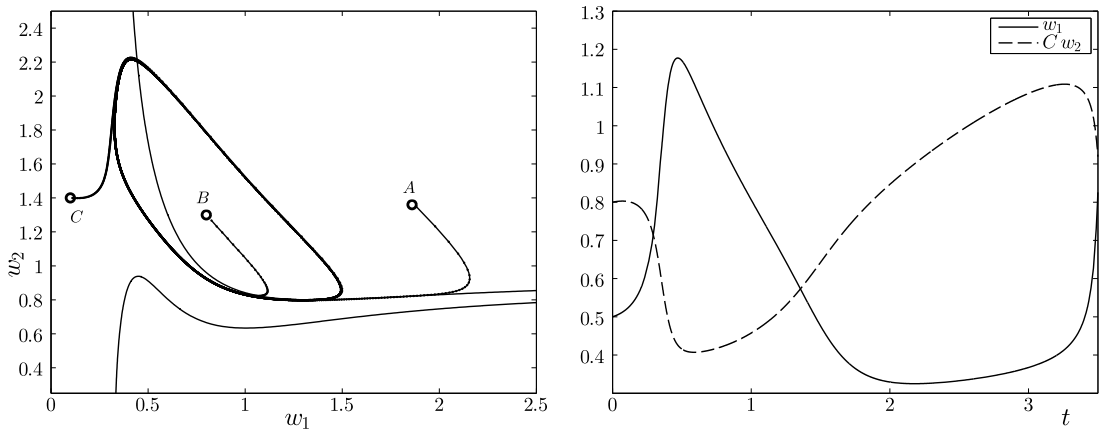


Fig. 3. Phase portrait of species w_1 , w_2 including typical nullclines and numerically computed trajectories of local kinetics starting from points A, B, C and reaching the origin (left) and reaction kinetics (right) for the Goldbeter model (4.4).

Here $v_1 = 1.58$ represents an inflow flux plus intracellular calcium pulses originated from the asynchrony of calcium pools receptors, $v_2 = 16$ and $v_3 = 91$ account for low and high levels of free cytosolic calcium flux pumped from the sarcoplasmic reticulum, and $v_4 = 2$ models an efflux of calcium out of the cell following a chemical exchange process. The remaining parameters are $v_5 = 0.2$, $k_2 = 1$, $k_3 = 4$, $k_4 = 0.93^4$. Only cytosolic calcium is assumed to diffuse, with anisotropy imposed by $\mathbf{D}_1 = \text{diag}(D_f, D_s, D_n)$ with $D_f = 60$, $D_s = 30$, $D_n = 30$, and $\mathbf{D}_2 = \mathbf{0}$. These parameter values lead to cyclic patterns on a fixed domain (see Fig. 3).

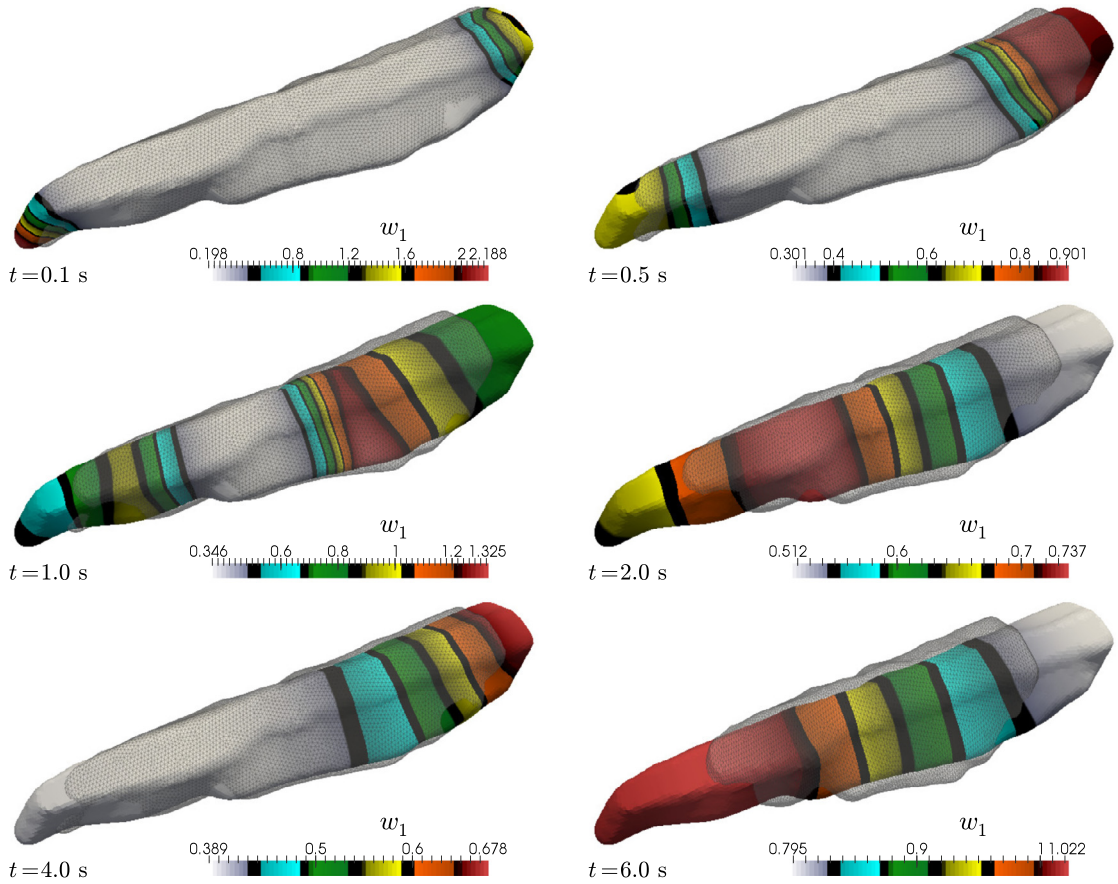


Fig. 4. Propagation of two calcium waves starting at the ends of a single cardiomyocyte. The employed mesh has 77 031 elements and 18 191 vertices. The superimposed hollow geometry represents the deformed configuration.

The material is assumed nonlinear mimicking the properties of living tissue, and we use an active stress approach to incorporate the influence of calcium (in this case, cytosolic calcium only) into the cell deformation. We propose to employ the following specification of the forcing term

$$\mathbf{f}(w_1) = \gamma \mathbf{f}_0 \otimes \mathbf{f}_0 \nabla w_1 + w_1 \mathbf{div}(\mathbf{f}_0 \otimes \mathbf{f}_0), \quad (4.5)$$

where \mathbf{f}_0 is a local unit vector denoting a known preferred direction of contraction in the myocyte reference configuration, and $\gamma = 0.25$ is an amplification factor. This term arises from an active stress of the form $\gamma w_1 \mathbf{f}_0 \otimes \mathbf{f}_0$. Robin boundary conditions are applied on the whole surface $\partial\Omega_0$. A tetrahedral mesh comprising 77 031 elements and 18 191 vertices (cf. [22]) is employed for the subsequent simulations (see initial fiber distribution in the top left panel of Fig. 6), where we observe the propagation of cytosolic calcium starting from initial sparks near the cell ends, and how it influences the contraction of the cell. Six snapshots of the evolution of calcium concentration w_1 are displayed in Fig. 4. We stress that all computations are purely Lagrangian, that is, elasticity and reaction equations are always solved in the reference configuration and the domain is moved according to the resulting deformations. Strains obtained directly from the mixed elasticity formulation are compared to those computed by numerical differentiation from a pure displacement computation. We can see from Fig. 5 a clear loss of accuracy, concentrated specially on the regions of high residual gradients. This issue illustrates the importance of computing strains directly, particularly when the interest lies in identifying zones of adhesion, or in determining provoked wall stresses. Further insight can be achieved from plotting transients of the computed solutions on a point near the cell mass center. Fig. 6 shows the evolution of calcium concentrations, displacement in all directions, and norm of the strain computed from numerical differentiation (test A) and from the mixed formulation (test B). A clear underestimation of strains and spurious oscillations are seen in test A with respect to the direct computation of test B, whereas calcium and displacements coincide in both tests.

Finally, we verify the optimal convergence of the numerical solution by looking at the quadratic decay of Newton-Raphson residuals associated to each field. Even though the results in Table 2 are provided for a single time step, a similar behavior is evidenced throughout the whole simulation.

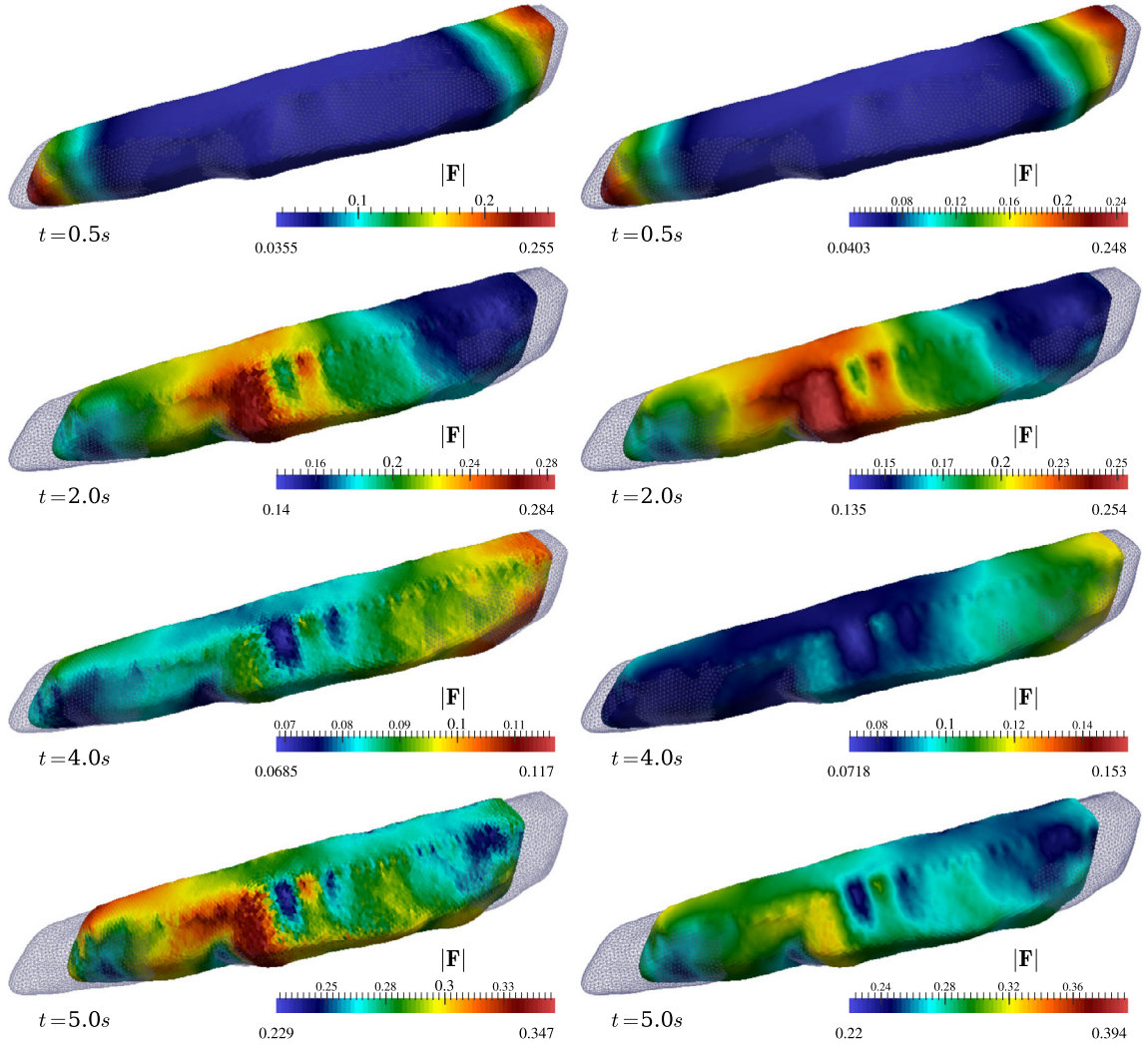


Fig. 5. Comparison of the time evolution of strains obtained via postprocessing from displacements (test A, left panels) and strains computed directly from the mixed formulation (test B, right panels). Here the hollow mesh represents the undeformed reference configuration.

4.3. Electric waves on slabs of excitable living tissue

We now turn to the simulation of potential propagation and its interaction with the deformable tissue. The specific model has been proposed in [46] and similar variants have been explored in e.g. [13]. The kinetics considered herein are

$$\begin{aligned} H_1(w_1, w_2) &= -kw_1(w_1 - a)(w_1 - 1) - w_1 w_2 + I_{\text{ext}}, \\ H_2(w_1, w_2) &= \left(c + \frac{d_1 w_2}{d_2 + w_1} \right) (-w_2 - kw_1(w_1 - b - 1)), \end{aligned} \quad (4.6)$$

where $a = b = 0.1$, $k = 8.0$, $c = 0.01$, $d_1 = 0.12$, and $d_2 = 0.3$ are dimensionless parameters and I_{ext} denotes a given time- or time- and space-dependent external stimulus. In this case the activation of the tissue deformation is encoded using the active-strain approach (see Remark 1) with an activation evolution dictated by

$$K(\gamma, w_2) = k_1 I_4(1 + \gamma)^3 + k_2 w_2, \quad (4.7)$$

where $k_1 = -0.3$, $k_2 = -2.4$. Reaction kinetics and a phase diagram are shown in Fig. 7.

The conductivity tensors for both species are taken isotropic $\mathbf{D}_i = D_i \mathbf{I}$ with $D_1 = 60$ and $D_2 = 50$. As in the previous example, the material is assumed Neo-Hookean incompressible with $\lambda = 1$, $\mu = 4000$, and the fibers direction is constant throughout the domain, aligned with the positive vertical axis $\mathbf{f}_0 = (0, 1)^T$. The undeformed computational domain consists of a square with boundaries of length 50 and centered in the origin, which has been discretized into 29 244 triangular

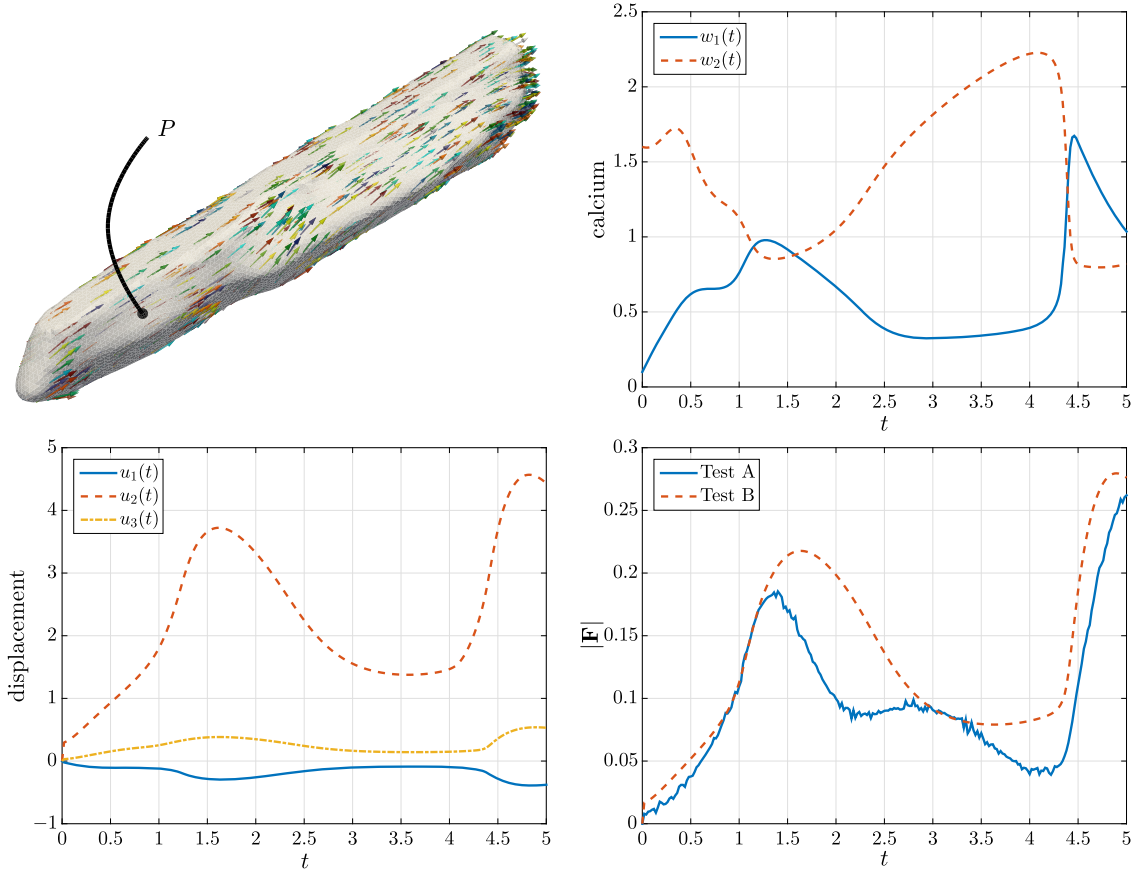


Fig. 6. Transients at a single point P on the myocyte boundary. Calcium concentrations (top right), displacement components (bottom left), and strains obtained via postprocessing from displacements (test A) or mixed formulation (test B) (bottom right).

Table 2

L^2 -norm of the residual vectors associated to the primal-mixed discretization of the single cell model, computed from time $t = 2 - \Delta t$ to $t = 2$ and stopped when reaching the tolerance $1e-8$.

Iter. number	$\ \text{res}(w_1)\ $	$\ \text{res}(w_2)\ $	$\ \text{res}(\sigma)\ $	$\ \text{res}(\mathbf{u})\ $	$\ \text{res}(p)\ $
1	7.0388e+1	4.1768e+1	1.9204e+1	3.7492e+0	6.7291e+0
2	1.3827e−2	3.7614e−2	4.0120e−2	1.1973e−1	8.8144e−1
3	2.7652e−4	5.8706e−4	6.8255e−4	3.8311e−3	1.9463e−3
4	1.6930e−5	2.9384e−6	5.7713e−6	7.0881e−5	7.2538e−5
5	1.1373e−7	3.5419e−7	1.0709e−7	2.6127e−7	9.5301e−8
6	3.3596e−9	1.9213e−9	5.4420e−9	6.2094e−9	8.4129e−9

elements and using 14 613 points. Robin conditions (with a bulk coefficient of 0.002) are enforced on the whole boundary. In order to onset the formation of spiral waves, a broken wave is considered as initial data [9]:

$$w_1(x, y, 0) = \begin{cases} -1 & \text{if } x \geq 0, y \geq 0, \\ 1 & \text{if } x < 0, y < 0, \\ 0 & \text{otherwise,} \end{cases} \quad w_2(x, y, 0) = \begin{cases} -1 & \text{if } x \leq 0, y \geq 0, \\ 1 & \text{if } x > 0, y < 0, \\ 0 & \text{otherwise.} \end{cases}$$

The timestep is set to $\Delta t = 0.001$, and the Newton tolerance is fixed to $1e-8$. Three snapshots illustrating the dynamics of the spatial distribution of species w_1 and the corresponding motion of the hyperelastic domain are displayed in the bottom panels of Fig. 8. For comparison purposes we have also included a computation of a fixed-domain example employing exactly the same reaction-diffusion model, indicating in this case a faster conduction of the field w_1 .

4.4. Cardiac electro-mechanics

We close this section with the application of the proposed primal-mixed finite element formulation in the numerical simulation of a simplified cardiac electromechanical problem. As in the previous examples, the tissue is assumed hyperelastic and anisotropic (with transverse isotropy across the fiber directions). The reaction-diffusion system corresponds to the

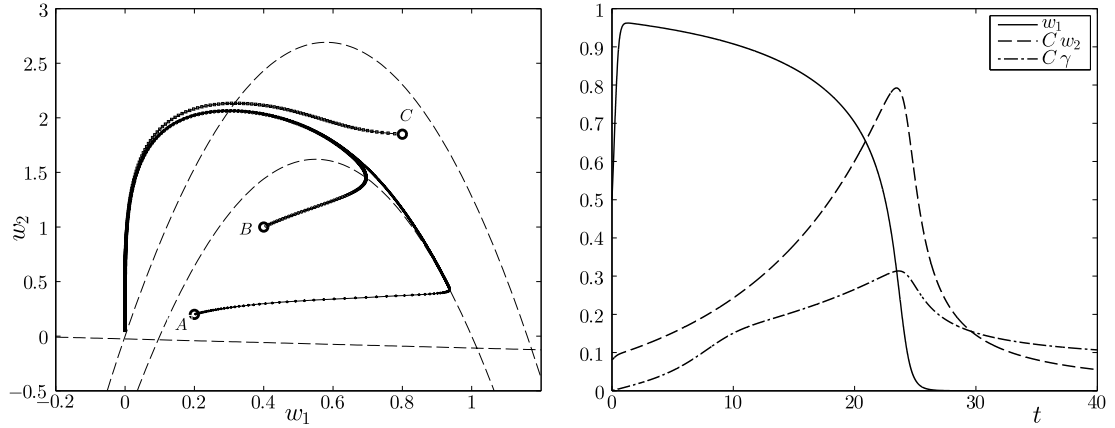


Fig. 7. Phase portrait of species w_1 , w_2 with nullclines and numerically computed trajectories starting from points A, B, C and reaching the origin (left); and reaction kinetics (right) for the Aliev–Panfilov model with mechanical activation based on local stretch and w_2 (4.6)–(4.7).

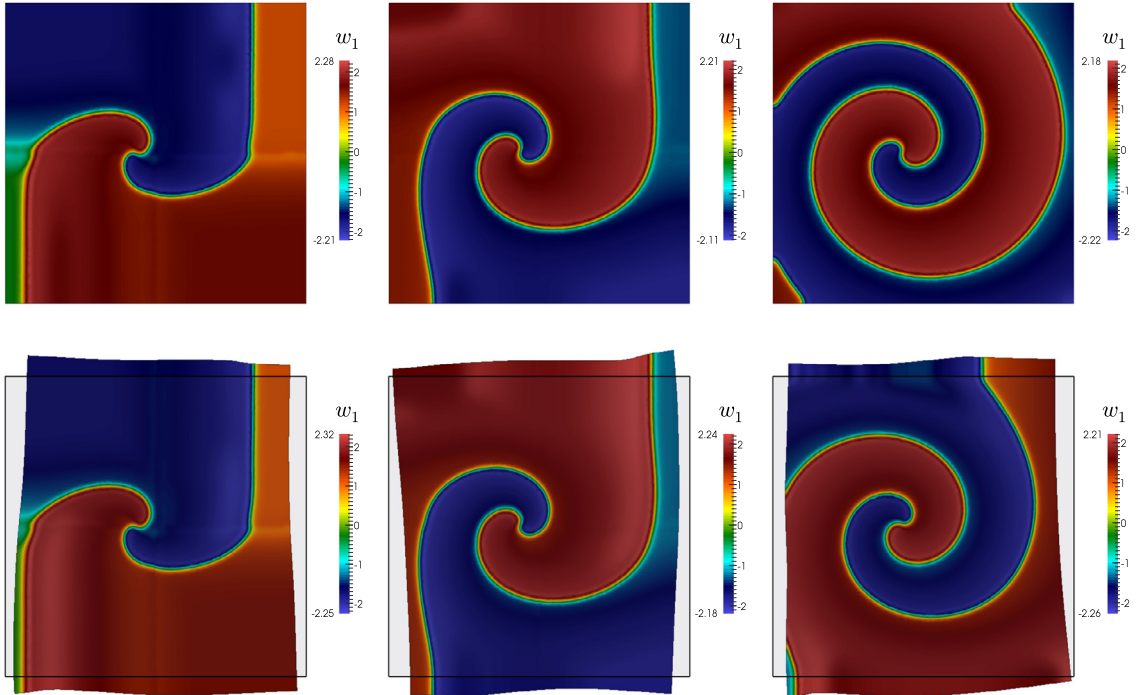


Fig. 8. Snapshots at time instants $t = 25, 50, 100$ of reentrant waves exhibited by species w_1 for a fixed (top) and a hyperelastic (bottom) slab.

monodomain equations incorporating the four-fields single cell model for human epicardial action potential proposed in [7], and characterized by $\mathbf{D}_2 = \mathbf{D}_3 = \mathbf{D}_4 = \mathbf{0}$ and the reaction terms

$$\begin{aligned}
 H_1(w_1, w_3, w_4) &= -w_2 H(w_1 - \theta_1)(w_1 - \theta_1)(w_v - w_1)/(\chi \tau_{fi}) - H(w_1 - \theta_2)w_3 w_4/(\chi \tau_{si}) \\
 &\quad + (w_1 - w_0)(1 - H(w_1 - \theta_2))/(\chi \tau_0) + H(w_1 - \theta_2)/(\chi \tau_{so}) + I_{ext}, \\
 H_2(w_1, w_2) &= (1 - H(w_1 - \theta_1))(w_{2,\inf} - w_2)/\tau_1^- - H(w_1 - \theta_1)w_2/\tau_1^+, \\
 H_3(w_1, w_3) &= (1 - H(w_1 - \theta_2))(w_{3,\inf} - w_3)/\tau_2^- - H(w_1 - \theta_2)w_3/\tau_2^+, \\
 H_4(w_1, w_4) &= ((1 + \tanh(k_3(w_1 - v_3)))/2 - w_4)/\tau_3,
 \end{aligned} \tag{4.8}$$

where H denotes the Heaviside function and the parameters are set as $v_0 = 0$, $v_v = 1.58$, $\theta_1 = 0.3$, $\theta_2 = 0.015$, $\theta_1^- = 0.015$, $\theta_0 = 0.006$, $\tau_{1,1}^- = 60$, $\tau_{1,2}^- = 1150$, $\tau_1^+ = 1.4506$, $\tau_{2,1}^- = 70$, $\tau_{2,2}^- = 20$, $k_2^- = 65$, $v_2^- = 0.03$, $\tau_2^+ = 280$, $\tau_{fi} = 0.11$, $\tau_{0,1} = 6$,

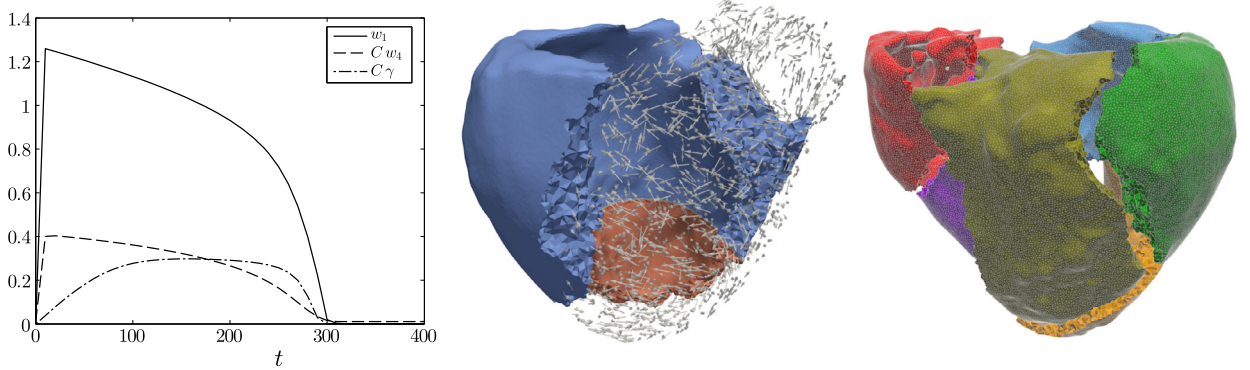


Fig. 9. Left: rescaled time evolution of the transmembrane potential w_1 , and calcium w_4 on a single point according to the Bueno–Orovio model (4.8), and activation field γ based on calcium, local stretch, and phenomenological force-length relations, governed by (4.9). Center: clipped biventricular geometry and generated fiber directions. Right: computational mesh partitioned into eight subdomains.

$\tau_{0,2} = 6$, $\tau_{s0,1} = 43$, $\tau_{s0,2} = 0.2$, $k_{s0} = 2$, $v_{s0} = 0.65$, $\tau_{3,1} = 2.7342$, $\tau_{3,2} = 3$, $k_3 = 2.0994$, $v_3 = 0.9087$, $\tau_{si} = 2.8723$, $\tau_{2,\infty} = 0.07$, $w_{2,\infty}^* = 0.94$. The constant initial conditions are $w_1(\mathbf{x}, 0) = 0$, $w_2(\mathbf{x}, 0) = w_3(\mathbf{x}, 0) = 1$, $w_4(\mathbf{x}, 0) = 0.02155$, and we employ a diffusion of $D_1 = 1.19 \text{ cm}^2/\text{s}$ for the first species.

Mechanical activation is imposed following the law derived in [48], which we modified accordingly to the transversely-isotropic case

$$K(\gamma, w_4) = F_A(w_4, I_4) + \sum_{i=1}^3 (-1)^i (i+1)(i+2) I_4 \gamma^i, \quad (4.9)$$

where $F_A(s, I_4) = (w_4 - w_{4,0})^2 R_{fl}(I_4)$, with $w_{4,0} = 0.2155$ and the force-length relationship R_{fl} introduced in [49]. The dynamics of w_1 , w_4 and γ are illustrated in Fig. 9, left. Robin boundary data are imposed on the whole epicardial boundary with coefficient $3.75 \text{ mmHg cm}^{-1}$, whereas the ventricular wall undergoes an initial pressure of 15 mmHg , and is let stress free afterwards. The computational domain (see Fig. 9, center and right panels) consists of a biventricular geometry discretized into 94 590 tetrahedral elements and 23 210 vertices, on which a rule-based algorithm has been used to generate a fiber field [48, Algorithm 1]. We employed a timestep of $\Delta t = 0.05 \text{ ms}$ and the external electric stimulus I_{ext} was applied after 5 ms on the half lower part of the right ventricle. Fig. 10 presents a series of snapshots of the propagation of species w_1 (the transmembrane potential) across the myocardium, and we also depict the corresponding deformed mesh according to the displacement field. We observe a milder contraction (both wall thickening and apex-base shortening) and a slightly lower conduction velocity than those reported in [48], which can be explained by differences in the activation mechanism model and the passive mechanical law (here we have restricted to Neo-Hookean materials, sheetlet directions have not been employed, and we do not discard the acceleration term in the momentum equation).

Let us point out that the influence of either a) postprocessing the strain tensor from the piecewise linear approximations of displacements, or b) computing it directly from the mixed formulation, not only affects the identification of high stress zones or other mechanisms directly related to strain computation, but also modifies substantially other indirectly related processes, such as the spatio-temporal behavior of the calcium field. Fig. 11 shows the dynamics of species w_4 in scenarios a) (top panels) and b) (bottom panels). Here we can readily observe qualitative differences in terms of calcium conduction velocity, that in turn, will inevitably have an impact in the transmembrane potential conduction velocity. For instance, the computations shown in the top panels yield a maximum conduction velocity of 59 cm/s for w_1 , whereas those associated to case b) imply a maximum conduction velocity of 72 cm/s , the latter being closer to the expected physiological value (87 cm/s) reported in [44].

5. Concluding remarks

In this paper we have introduced a primal-mixed formulation for the two-way coupling of nonlinear reaction-diffusion equations and linear/nonlinear elasticity. A flexible and robust mixed finite element method has been proposed, which follows the same structure as the continuous formulation, and where the main advantage with respect to the methods introduced in [1,4] is the possibility of recovering with the desired accuracy the strain (deformation gradient) needed in the modified diffusion of the reaction-diffusion system, and, as usual in mixed methods, the restrictions on the finite element spaces associated to the elasticity equations can be relaxed. The proposed formulation has been structured so that it fits in the study of some typical scenarios in biological systems where the reactions affect directly the material displacements through either active stress or active strain models. The numerical scheme has been validated in terms of spatio-temporal accuracy of approximate solutions, and a few examples related to cardiac biomechanics were provided to illustrate its feasibility.

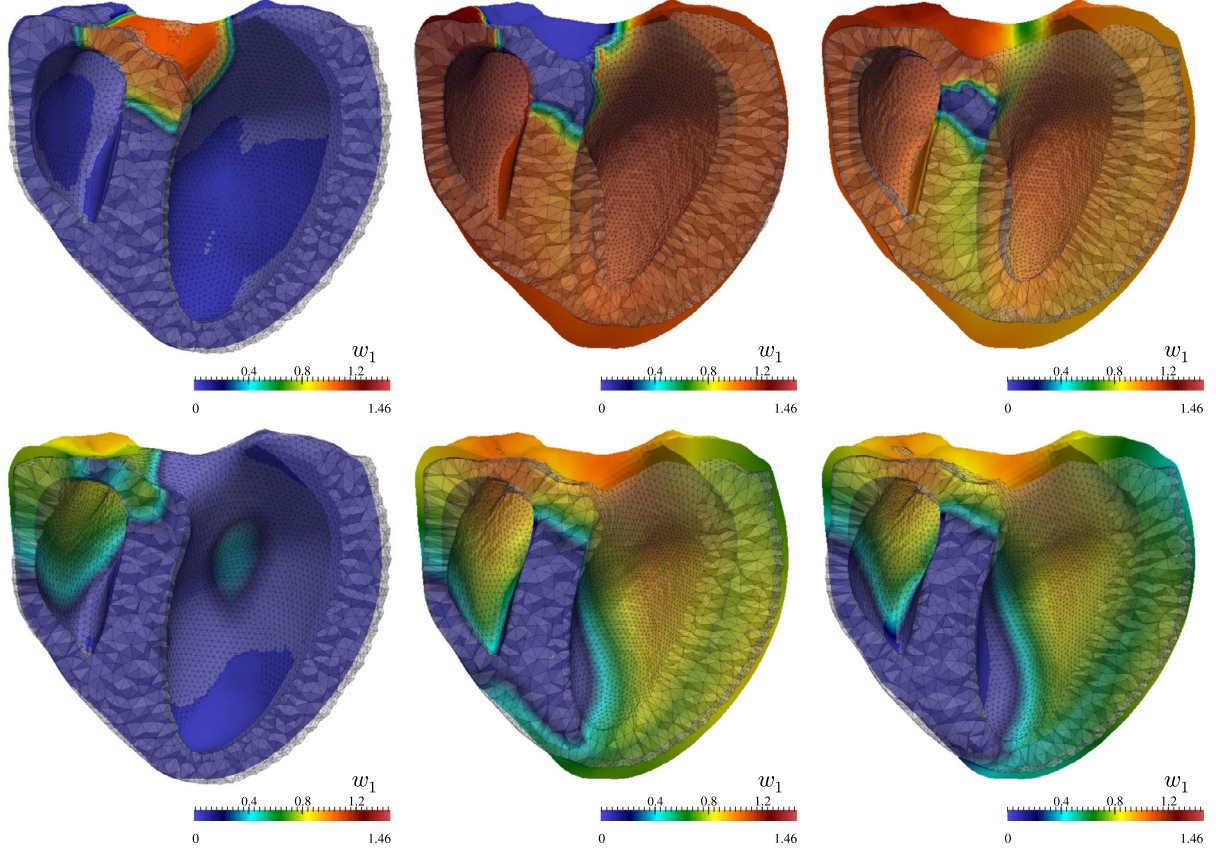


Fig. 10. Clipped snapshots of transmembrane potential w_1 and cut of the deformed mesh at time instants $t = 100, 300, 500, 700, 900, 1100$ ms.

While this paper has focused on relatively simple cases, model complexity can be readily increased so that the present framework can be straightforwardly employed in the control of a larger class of problems and more involved (not necessarily biological) processes such as chemical reactions in fully-saturated rigid porous skeletons [17], and its extension to the case of deformable porous media. Many other ingredients can be added, for instance material orthotropy or statistical properties of fiber families [56], or multiscale descriptions. We stress that our model for the way that species' concentration affects the motion of the tissue (for instance, (4.5)) depends strongly on the specific application, which leaves plenty of room for further investigation, especially in terms of restrictions imposed by the second law of thermodynamics and other aspects related to energy-derived mechanical activation [48,49] (see also Remark 1). Notice that remeshing is not performed in the present case, since the proposed formulation is entirely Lagrangian and the numerical solution is carried out using a fixed mesh on the reference configuration. Nevertheless, special techniques to enforce mesh quality during large body deformations may become essential if we couple the present framework with Eulerian descriptions of flow (e.g. in cardiac mechano-electrical-fluidic models), where mesh motion of the fluid domain may lead to highly distorted elements. A recent remedy, based on adaptive smoothing and remeshing is presented in [39].

Further lines of development also include HPC-related questions such as scalability of solvers and construction of smart preconditioners. Finally, we mention that the development of fully mixed formulations for (2.9) and their convergence analysis will be the subject of a separate contribution.

Acknowledgements

The support by the Swiss National Science Foundation through the grant SNSF PP00P2-144922 is gratefully acknowledged. Special thanks are also due to Alessio Gizzi (Campus Bio-Medico, Rome), Aymen Laadhari (ETH Zurich), Toni Lassila (Sheffield University), Alfio Quarteroni (EPF Lausanne), and Simone Rossi (Duke University) for kindly providing the single cell and heart geometries, and for the numerous stimulating discussions on the subject of cardiac biomechanics. Finally, we thank the suggestions by two anonymous reviewers, which yielded substantial improvements with respect to the initial version of this manuscript.

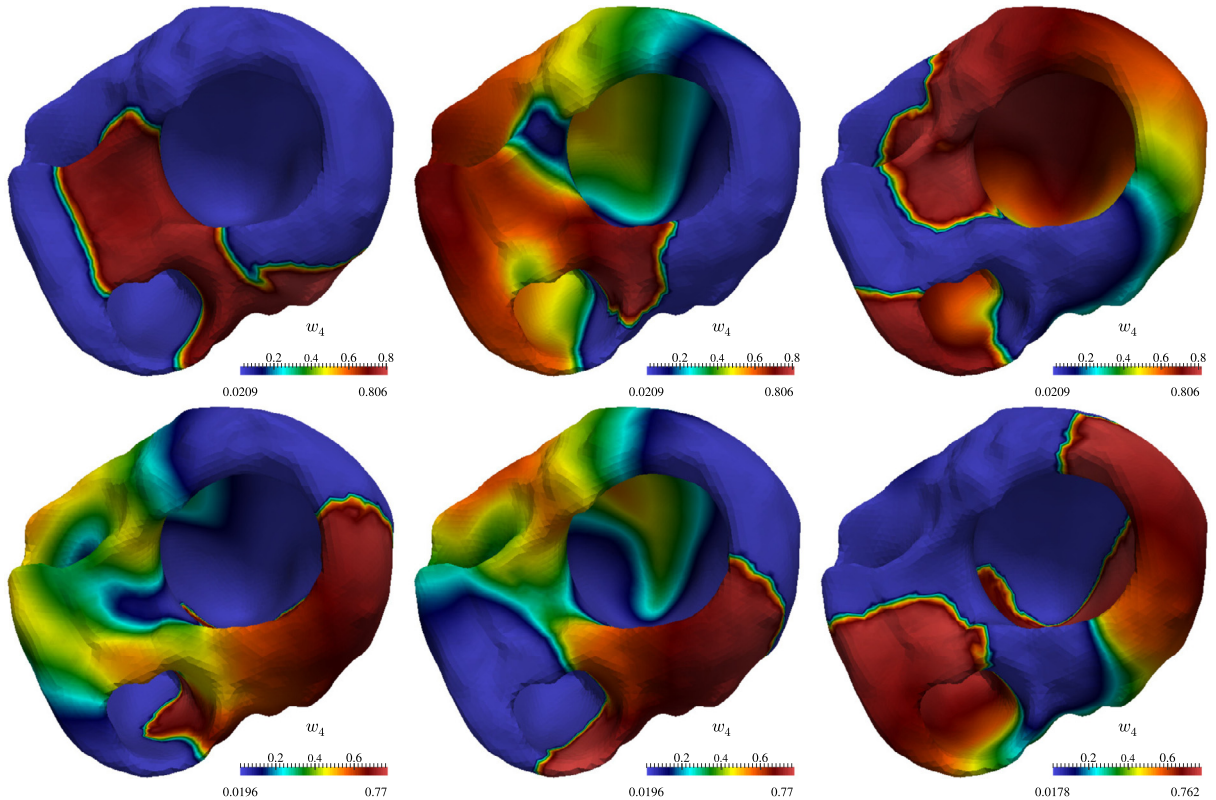


Fig. 11. Snapshots of reentrant waves in species w_4 at times $t = 20, 150, 300$ ms for the case of strains obtained via numerical differentiation from piecewise linear approximation of displacements (top), and strains computed directly from the mixed formulation (bottom panels).

References

- [1] B. Andreianov, M. Bendahmane, A. Quarteroni, R. Ruiz-Baier, Solvability analysis and numerical approximation of linearized cardiac electromechanics, *Math. Models Methods Appl. Sci.* 25 (2015) 959–993.
- [2] R.P. Araujo, D.L.S. McElwain, A mixture theory for the genesis of residual stresses in growing tissues. II. Solutions to the biphasic equations for a multicell spheroid, *SIAM J. Appl. Math.* 66 (2005) 447–467.
- [3] D. Baroli, A. Quarteroni, R. Ruiz-Baier, Convergence of a stabilized discontinuous Galerkin method for incompressible nonlinear elasticity, *Adv. Comput. Math.* 39 (2013) 425–443.
- [4] R. Barreira, C.M. Elliott, A. Madzvamuse, The surface finite element method for pattern formation on evolving biological surfaces, *J. Math. Biol.* 63 (2011) 1095–1119.
- [5] M. Bergdorf, I.F. Sbalzarini, P. Koumoutsakos, A Lagrangian particle method for reaction–diffusion systems on deforming surfaces, *J. Math. Biol.* 61 (2010) 649–663.
- [6] J. Bonet, R.D. Wood, *Nonlinear Continuum Mechanics for Finite Element Analysis*, second ed., Cambridge University Press, Cambridge, 2008.
- [7] A. Bueno-Orovio, E.M. Cherry, F.H. Fenton, Minimal model for human ventricular action potentials in tissue, *J. Theor. Biol.* 253 (2008) 544–560.
- [8] A. Buganza Tepole, E. Kuhl, Computational modeling of chemo-bio-mechanical coupling: a systems-biology approach towards wound healing, *Comput. Methods Biomed. Eng.* 24 (2014) 1–18.
- [9] R. Bürger, R. Ruiz-Baier, K. Schneider, Adaptive multiresolution methods for the simulation of waves in excitable media, *J. Sci. Comput.* 43 (2010) 261–290.
- [10] M.A.J. Chaplain, M. Ganesh, I.G. Graham, Spatio-temporal pattern formation on spherical surfaces: numerical simulation and application to solid tumour growth, *J. Math. Biol.* 42 (2001) 387–423.
- [11] K.S. Chavan, B.P. Lamichhane, B.I. Wohlmuth, Locking-free finite element methods for linear and nonlinear elasticity in 2D and 3D, *Comput. Methods Appl. Mech. Eng.* 196 (2007) 4075–4086.
- [12] S. Chen, Y.-T. Zhang, Krylov implicit integration factor methods for spatial discretization on high dimensional unstructured meshes: application to discontinuous Galerkin methods, *J. Comput. Phys.* 230 (2011) 4336–4352.
- [13] C. Cherubini, S. Filippi, P. Nardinocchi, L. Teresi, An electromechanical model of cardiac tissue: constitutive issues and electrophysiological effects, *Prog. Biophys. Mol. Biol.* 97 (2008) 562–573.
- [14] E.J. Crampin, E.A. Gaffney, P.K. Maini, Reaction and diffusion on growing domains: scenarios for robust pattern formation, *Bull. Math. Biol.* 61 (1999) 1093–1120.
- [15] S.K. Dasika, S.T. Kinsey, B.R. Locke, Reaction–diffusion constraints in living tissue: effectiveness factors in skeletal muscle design, *Biotechnol. Bioeng.* 108 (2011) 104–105.
- [16] R. FitzHugh, Impulses and physiological states in theoretical models of nerve membrane, *Biophys. J.* 1 (1961) 445–465.
- [17] G. Galiano, J. Velasco, Competing through altering the environment: a cross-diffusion population model coupled to transport–Darcy flow equations, *Nonlinear Anal., Real World Appl.* 12 (2011) 2826–2838.
- [18] G.N. Gatica, Analysis of a new augmented mixed finite element method for linear elasticity allowing $\mathbf{RT}_0\text{-}\mathbf{P}_1\text{-}\mathbf{P}_0$ approximations, *M2AN Math. Model. Numer. Anal.* 40 (2006) 1–28.

- [19] G.N. Gatica, A Simple Introduction to the Mixed Finite Element Method. Theory and Applications, Springer-Verlag, Berlin, 2014.
- [20] G.N. Gatica, N. Heuer, S. Meddahi, On the numerical analysis of nonlinear twofold saddle point problems, *IMA J. Numer. Anal.* 23 (2003) 301–330.
- [21] A. Gizzi, C. Cherubini, S. Filippi, A. Pandolfi, Theoretical and numerical modeling of nonlinear electromechanics with applications to biological active media, *Commun. Comput. Phys.* 17 (2015) 93–126.
- [22] A. Gizzi, R. Ruiz-Baier, S. Rossi, A. Laadhari, C. Cherubini, S. Filippi, A three-dimensional continuum model for active contraction in single cardiomyocytes, in: A. Quarteroni (Ed.), *Modeling the Heart and the Circulatory System*, in: *Model. Simul. Appl.*, vol. 14, Springer-Verlag, Milano, 2015, pp. 157–176.
- [23] S. Göktepe, E. Kuhl, Electromechanics of the heart: a unified approach to the strongly coupled excitation–contraction problem, *Comput. Mech.* 45 (2010) 227–243.
- [24] A. Goldbeter, G. Dupont, M.J. Berridge, Minimal model for signal-induced Ca^{2+} oscillations and for their frequency encoding through protein phosphorylation, *Proc. Natl. Acad. Sci. USA* 87 (1990) 1461–1465.
- [25] P. Gray, S.K. Scott, Autocatalytic reactions in the isothermal, continuous stirred tank reactor: oscillations and the instabilities in the system $A + 2B \rightarrow 3B$, $B \rightarrow X$, *Chem. Eng. Sci.* 39 (1984) 1087–1097.
- [26] E. Hairer, S.P. Nørsett, G. Wanner, Solving Ordinary Differential Equations. I: Nonstiff Problems, second ed., Springer Ser. Comput. Math., Springer-Verlag, Berlin, 1993.
- [27] M. Holzer, A. Doelman, T.J. Kaper, Existence and stability of traveling pulses in a reaction–diffusion–mechanics system, *J. Nonlinear Sci.* 23 (2013) 129–177.
- [28] J.S. Howell, N.J. Walkington, Inf-sup conditions for twofold saddle point problems, *Numer. Math.* 118 (2011) 663–693.
- [29] D.E. Hurtado, D. Henao, Gradient flows and variational principles for cardiac electrophysiology: toward efficient and robust numerical simulations of the electrical activity of the heart, *Comput. Methods Appl. Mech. Eng.* 273 (2014) 238–254.
- [30] J. Kelkel, C. Surulescu, A weak solution approach to a reaction–diffusion system modeling pattern formation on seashells, *Math. Methods Appl. Sci.* 32 (2009) 2267–2286.
- [31] R.C.P. Kerckhoffs, S.N. Healy, T.P. Usyk, A.D. McCulloch, Computational methods for cardiac electromechanics, *Proc. IEEE* 94 (2006) 769–783.
- [32] E. Kuhl, Growing matter – a review of growth in living systems, *J. Mech. Behav. Biomed. Mater.* 29 (2014) 529–543.
- [33] A. Laadhari, R. Ruiz-Baier, A. Quarteroni, Fully Eulerian finite element approximation of a fluid–structure interaction problem in cardiac cells, *Int. J. Numer. Methods Eng.* 96 (2013) 712–738.
- [34] S. Lamparter, Y. Sun, K.T. Weber, Angiotensin II receptor blockade during gestation attenuates collagen formation in the developing rat heart, *Cardiovasc. Res.* 43 (1999) 165–172.
- [35] P. Le Tallec, Existence and approximation results for nonlinear mixed problems: application to incompressible finite elasticity, *Numer. Math.* 38 (1981/1982) 365–382.
- [36] V.A. Lubarda, Constitutive theories based on the multiplicative decomposition of deformation gradient: thermoelasticity, elastoplasticity and biomechanics, *Appl. Mech. Rev.* 57 (2004) 95–108.
- [37] A. Madzvamuse, P.K. Maini, Velocity-induced numerical solutions of reaction–diffusion systems on continuously growing domains, *J. Comput. Phys.* 225 (2007) 100–119.
- [38] S.A. Meier, A. Muntean, A two-scale reaction–diffusion system with micro-cell reaction concentrated on a free boundary, *C. R., Méc.* 336 (2008) 481–486.
- [39] S. Menon, K.G. Mooney, K.G. Staph, D.P. Schmidt, Parallel adaptive simplicial re-meshing for deforming domain CFD computations, *J. Comput. Phys.* 298 (2015) 62–78.
- [40] V. Mironov, T. Boland, T. Trusk, G. Forgacs, R.R. Markwald, Organ printing: computer-aided jet-based 3D tissue engineering, *Trends Biotechnol.* 21 (2003) 157–161.
- [41] Y. Morishita, Y. Iwasa, Growth based morphogenesis of vertebrate limb bud, *Bull. Math. Biol.* 70 (2008) 1957–1978.
- [42] C. Murea, H.G.E. Hentschel, A finite element method for growth in biological development, *Math. Biosci. Eng.* 4 (2007) 339–353.
- [43] J.S. Nagumo, S. Arimoto, S. Yoshizawa, An active pulse transmission line stimulating nerve axon, *Proc. Inst. Radio Eng.* 50 (1962) 2061–2071.
- [44] K. Nanthakumar, J. Jalife, S. Masse, E. Downar, M. Pop, J. Asta, H. Ross, V. Rao, S.F. Mironov, E. Sevaptsidis, J.M. Rogers, G. Wright, R. Dhopeshwarkar, Optical mapping of Langendorff perfused human hearts: establishing a model for the study of ventricular fibrillation in humans, *Am. J. Physiol.* 293 (2007) H875–H880.
- [45] P. Nardinocchi, L. Teresi, On the active response of soft living tissues, *J. Elast.* 88 (2007) 27–39.
- [46] M.P. Nash, A.V. Panfilov, Electromechanical model of excitable tissue to study reentrant cardiac arrhythmias, *Prog. Biophys. Mol. Biol.* 85 (2004) 501–522.
- [47] F. Nobile, A. Quarteroni, R. Ruiz-Baier, An active strain electromechanical model for cardiac tissue, *Int. J. Numer. Methods Biomed. Eng.* 28 (2012) 52–71.
- [48] S. Rossi, T. Lassila, R. Ruiz-Baier, A. Sequeira, A. Quarteroni, Thermodynamically consistent orthotropic activation model capturing ventricular systolic wall thickening in cardiac electromechanics, *Eur. J. Mech. A, Solids* 48 (2014) 129–142.
- [49] R. Ruiz-Baier, A. Gizzi, S. Rossi, C. Cherubini, A. Laadhari, S. Filippi, A. Quarteroni, Mathematical modelling of active contraction in isolated cardiomyocytes, *Math. Med. Biol.* 31 (2014) 259–283.
- [50] M.D. Ryser, S.V. Komarova, N. Nigam, The cellular dynamics of bone remodeling: a mathematical model, *SIAM J. Appl. Math.* 70 (2010) 1899–1921.
- [51] J. Schnakenberg, Simple chemical reaction systems with limit cycle behavior, *J. Theor. Biol.* 81 (1979) 389–400.
- [52] M.J. Simpson, K.A. Landman, D.F. Newgreen, Chemotactic and diffusive migration on a nonuniformly growing domain: numerical algorithm development and applications, *J. Comput. Appl. Math.* 192 (2006) 282–300.
- [53] L.A. Taber, R. Perucchio, Modeling heart development, *J. Elast.* 61 (2000) 165–197 (2001).
- [54] G. Tauriello, P. Koumoutsakos, Coupling remeshed particle and phase field methods for the simulation of reaction–diffusion on the surface and the interior of deforming geometries, *SIAM J. Sci. Comput.* 35 (2013) B1285–B1303.
- [55] A.M. Turing, The chemical basis of morphogenesis, *Philos. Trans. R. Soc. Lond. B* 237 (1952) 37–72.
- [56] M. Vasta, A. Gizzi, A. Pandolfi, On three- and two-dimensional fiber distributed models of biological tissues, *Probab. Eng. Mech.* 37 (2014) 170–179.
- [57] B.L. Vaughan, R.E. Baker, D. Kay, P.K. Maini, A modified Oster–Murray–Harris mechanical model of morphogenesis, *SIAM J. Appl. Math.* 73 (2013) 2124–2142.
- [58] L.D. Weise, M.P. Nash, A.V. Panfilov, A discrete model to study reaction–diffusion–mechanics systems, *PLoS ONE* 6 (2011) e21934.
- [59] J.P. Whiteley, Discontinuous Galerkin finite element methods for incompressible non-linear elasticity, *Comput. Methods Appl. Mech. Eng.* 198 (2009) 3464–3478.
- [60] S.-Y. Yi, Convergence analysis of a new mixed finite element method for Biot's consolidation model, *Numer. Methods Partial Differ. Equ.* 30 (2014) 1189–1210.
- [61] J. Zhu, Y.-T. Zhang, M. Alber, S. Newman, Bare bones pattern formation: a core regulatory network in varying geometries reproduces major features of vertebrate limb development and evolution, *PLoS ONE* 5 (2010) e10892.
- [62] J. Zhu, Y.-T. Zhang, S. Newman, M. Alber, A finite element model based on discontinuous Galerkin methods on moving grids for vertebrate limb pattern formation, *Math. Model. Nat. Phenom.* 4 (2009) 131–148.